

1 **I do not have tracked changes because most of the manuscript has been rewritten. Key**
2 **revisions are to the Introduction, Conclusion and Sections 2 and 3. All other sections have**
3 **also been heavily modified to help streamline the paper. Section 4 is new. The notation section**
4 **(Section 8) is also new.**

6 **A landslide runout model for sediment transport, landscape** 7 **evolution and hazard assessment applications**

8 Jeffrey Keck^{1,2}, Erkan Istanbuluoglu¹, Benjamin Campforts³, Gregory Tucker^{4,5}, Alexander
9 Horner-Devine¹

10 ¹ University of Washington, Civil and Environmental Engineering, Seattle, WA, USA

11 ² Washington Department of Natural Resources, Forest Resources Division, Olympia, WA, USA

12 ³ Institute of Arctic and Alpine Research, University of Colorado Boulder, Boulder, CO, USA

13 ⁴ Department of Geological Sciences, University of Colorado Boulder, Boulder, CO, USA

14 ⁵ Cooperative Institute for Research in Environmental Sciences (CIRES), University of Colorado Boulder, Boulder,
15 CO, USA

16
17 *Correspondence to:* Jeffrey Keck (keckje@gmail.com)

18 Abstract

19 We developed a new rule-based, cellular-automaton algorithm for predicting the hazard extent, sediment transport and
20 topographic change associated with the runout of a landslide. This algorithm, which we call MassWastingRunout
21 (MWR), is coded in Python and implemented as a component for the package Landlab. MWR combines the
22 functionality of simple runout algorithms used in landscape evolution and watershed sediment yield models with the
23 predictive details typical of runout models used for landslide inundation hazard mapping. An initial DEM, a regolith
24 depth map, and the location polygon of a landslide are the only inputs required to run MWR to model the entire runout
25 process. MWR runout incorporates rules of mass conservation, erosion and deposition, which are driven by
26 topography. For the purpose of facilitating rapid calibration to a site, MWR includes a calibration utility that uses a
27 Markov Chain Monte Carlo algorithm to automatically calibrate the model to match observed runout extent, deposition
28 and erosion. Output from the calibration utility can be used to inform probabilistic implementation of MWR. Here we
29 use a series of synthetic terrains to demonstrate basic model response to topographic convergence and slope, test
30 calibrated model performance relative to several observed landslides, and briefly demonstrate how MWR can be used
31 to develop a probabilistic runout hazard map. A calibrated runout model may allow for region-specific and more
32 insightful predictions of landslide impact on landscape morphology and watershed-scale sediment dynamics, and
33 should be further investigated in future modelling studies.

34 1. Introduction

35 Over geologic timescales, landslides and their runout shape the topographic expression of mountain ranges and
36 channel networks (e.g., Campforts et al., 2022; Korup, 2006; Larsen and Montgomery, 2012; Montgomery and
37 Dietrich, 1988). Over more pragmatic engineering and environmental risk management timescales, landslides and
38 their runout can inundate and destroy infrastructure (e.g., Kean et al., 2019) but also support numerous ecosystem
39 benefits, including carbon and nutrient transport from hillslopes to channels and the creation of riparian habitat (Benda
40 et al., 2003; Bigelow et al., 2007; Goode et al., 2012). Therefore, explicit representation of landslide runout is a
41 necessary component of: (1) landslide inundation hazard assessments, with emphasis on inundation extent and flow
42 depth (e.g., Frank et al. 2015, Han et al., 2015); (2) watershed sediment yield models, with emphasis on the
43 mobilization, deposition and type of sediment carried by the landslide (e.g., Bathurst and Burton, 1998;
44 Istanbuluoglu, et al., 2005); and (3) landscape evolution models, with emphasis on topographic change prediction
45 (e.g., Tucker and Bras, 1998; Istanbuluoglu and Bras, 2005; Campforts et al., 2022);

46 Landslide runout processes can be generalized into three phases: initiation, erosion, and deposition. After a landslide
47 initiates, it may break apart and flow as a relatively dry debris slide, or it may mix with surface runoff to become a
48 debris flow. The mobility of the mass wasting material and resulting erosion/deposition pattern often varies as a
49 function of runout topography and initial relief and size of the landslide (Iverson, 1997). Mobility may also be
50 impacted by substrate liquefaction (Hung and Evans, 2004) and landslide basal cataclasis (Shaller et al. 2020). As
51 the runout material moves downslope, flow depth varies as a function of channel width (Kean et al, 2019), which in
52 turn impacts erosion rates (Schürch et al. 2011). Theoretical, field and laboratory observations indicate that erosion
53 rates may also depend on the moisture content of the channel bed (Iverson, 2012; McCoy et al. 2012), flow grainsize
54 (Egashira et al., 2001) and granular stress within the flow (Capart et al, 2015). The slope at which deposition begins
55 is controlled by the grain to water ratio and friction angle of the slide material (Takahashi, 2014; Major and Iverson,
56 1999; Zhou et al., 2019) but the friction angle of the material may vary as a function of the grains in the flow and
57 fluidization of the flow material (Hutter et al., 1996). Lateral levees often form along the edges of the flow (Major,
58 1997; Whipple and Dunne, 1992; Shaller et al., 2020) and deposition at the distal end of the flow may occur as layered
59 accretion (Major, 1997) or as the emplacement of a single, massive deposit (Shaller et al., 2020). If the water content
60 of the runout material is high enough, as the solid fraction of the distal end of the flow compresses, the water is
61 squeezed out and may continue as an immature debris flow (sensu Takahashi, 2014) or intense bedload (sensu Capart
62 & Fraccarolo, 2011), extending the runout distance (e.g., Shaller et al. 2020).

63 Landslide inundation hazard models aim to accurately predict the runout extent and/or flow depths of a runout event
64 and may include some or most of the above processes in the model. Example models include: (1) site-specific-
65 empirical/statistical models that use simple geometric rules and an estimate of the total mobilized volume (initial
66 landslide + eroded volume) or a growth factor (e.g., Reid et al. 2016); (2) detailed, continuum-based mechanistic
67 models, which conceptualize the runout process as a single-phase or multiphase flow using the depth-integrated
68 Navier-Stokes equations for an incompressible, free-surface flow (i.e., shallow water equations; Frank et al, 2015;
69 Han et al., 2015; Iverson and Denlinger, 2001) and often (though not always) require pre-knowledge of the total
70 mobilized volume (e.g., Barnhart et al., 2021; Han et al. 2015); (3) reduced-complexity flow-routing models that use

71 rule-based abstractions of the key physical processes that control the flow (Clerici and Perego, 2000; Guthrie and
72 Befus, 2021; Gorr et al., 2022; Han et al., 2017, 2021; Horton et al., 2013; Liu et al., 2022) and are typically
73 implemented using just the initial landslide location and volume but often rely on heavy, site specific parameterization
74 and; (4) hybrid modelling approaches that combine mechanistic models with empirical and reduced-complexity
75 approaches (D'Ambrosio et al., 2003; Iovine et al., 2005; Lancaster et al., 2003; McDougall and Hungr 2004; Medina
76 et al., 2008).

77 For landscape evolution and watershed sediment yield applications (herein referred to as watershed sediment models,
78 WSMs), the runout model must be scalable in both space and time, and use internally modelled landslide location and
79 size (e.g. Tucker and Bras, 1998; Doten et al 2006; Campforts et al. 2022). As such, computationally efficient and
80 parsimonious reduced complexity runout models that evolve the terrain and transfer sediment are often preferred in
81 WSMs, however with simplifications that can restrict model ability to accurately replicate observed inundation extent
82 or depositional patters. Such simplifications include omitting debris flow erosion and bulking in runout channels,
83 limiting flow to only a single cell in the steepest downstream direction, and assuming debris flows only occupy the
84 width of a single cell (e.g., Tucker and Bras, 1998; Istanbuluoglu and Bras, 2005) or link of a channel network (Benda
85 and Dunne, 1997).

86 To bridge the scalable functionality of WSMs with the predictive accuracy of landslide inundation hazard models,
87 without the computational overhead of a detailed mechanistic representation of the runout process, or difficult
88 parameterization typical of other models, we developed a new, reduced-complexity landslide runout model, called
89 MassWastingRunout (MWR). MWR models landslide runout starting from the source area of the landslide, making it
90 easily compatible with WSMs that internally determine landslide area and location. MWR tracks sediment transport
91 and topographic change downstream, and evolves the attributes of the transport material. MWR can be calibrated by
92 adjusting just two parameters and is augmented with a Markov Chain Monte Carlo (MCMC) calibration utility that
93 automatically parameterizes model behavior to observed runout characteristics (e.g., erosion, deposition, extent).
94 MWR also includes a built-in utility called MWR Probability, designed for running an ensemble of simulations to
95 develop probabilistic debris flow hazard maps.

96 In this paper, we present the conceptualization and numerical implementation of the MWR model (Section 2), describe
97 the calibration utility and its probabilistic implementation (Section 3) and demonstrate basic model response to
98 topographic convergence and slope on a series of synthetic terrains (Section 4). Event-scale applications to replicate
99 observed runout extent, sediment transport, and topographic change at four topographically and geologically unique
100 field sites are discussed (Figure 1; described in Section 5). We test MWR's predictive ability using the
101 parameterization of one site to predict runout hazard at a nearby site and show a brief example of Monte Carlo model
102 runs to determine runout probability from a hydrologically-driven landslide hazard map or an expert-determined
103 potentially unstable slope (Section 6). We conclude with a short summary of MWR model performance and discuss
104 how a calibrated MWR can be incorporated into WSMs.



105

106 **Figure 1:** Example landslides that are used to evaluate calibrated MWR performance: (a) Cascade Mountains, WA: a large debris
 107 avalanche over steep, broadly convergent terrain (photo credit: Stephen Slaughter). (b) Black Hills, WA: large debris flows over a
 108 broadly convergent, gently sloped valley (photo credit: Stephen Slaughter). (c) Rocky Mountains, CO: a moderate sized debris
 109 avalanche over steep, unconfined to divergent hillslope. (d) Olympic Mountains, WA: small debris flows in steep, highly
 110 convergent channels.

111 **2. Description of the MassWastingRunout model**

112 **2.1 Overview of the cellular-automaton Modelling approach**

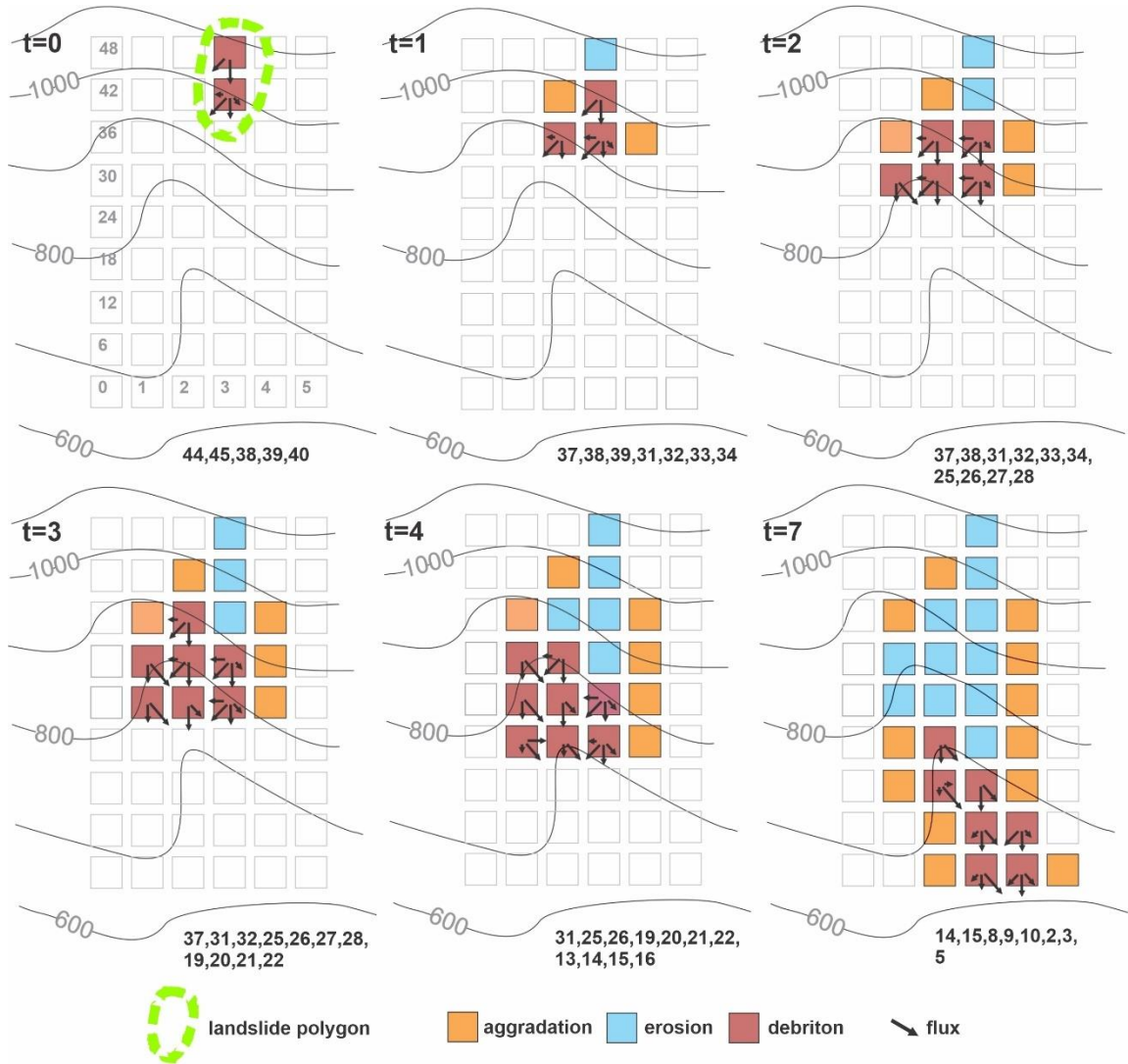
113 MWR is coded as a discrete cellular automaton (CA) model. CA models apply a set of equations or rules (deterministic
 114 or probabilistic) to individual cells of a grid to change the numerical or categorical value of a cell state (e.g., Codd,
 115 1968). In earth sciences, CA models are widely used to model everything from vegetation dynamics (e.g., Nudurupati
 116 et al., 2023) to lava flows (e.g., Barca et al., 1993) to geomorphic transport, in which gravitationally directed erosion
 117 and depositional processes modify a digital elevation model (DEM) representation of a landscape (e.g., Chase, 1992;

118 Crave & Davy, 2001; Murray & Paola, 1994; Tucker et al., 2018). Existing CA-based landslide runout models include
119 Guthrie and Befus (2021), D’Ambrosio et al. (2003) and Han et al. (2021). In all of these models, runout behavior is
120 controlled by topographic slope and rules for erosion and deposition but conceptualization and implementation differ.
121 In MWR, mass-continuity is central to model conceptualization. Of the wide range of processes described in the
122 introduction that control observed runout, MWR explicitly represents erosion, deposition, and flow resistance due to
123 debris size and vegetation. Material exchange between the runout material and underlying terrain as well as flow
124 resistance determines runout extent and landscape evolution. Model rules are designed such that they can be
125 parameterized from field measurements. Finally, in MWR, most computations occur only at the location of moving
126 debris, in a manner analogous to the “mobile” cellular automaton implementation of Chase (1992).
127 Chase (1992) modelled precipitation-driven surface erosion by randomly placing single packets of precipitation on a
128 DEM, which then moved from higher elevation to lower elevation grid cells, eroding and transporting sediment as a
129 function of the slope between the cells. The individual packets of precipitation were referred to as precipitons. In
130 MWR, since we route the downslope progression of debris from a specified mass wasting source area, we refer to
131 these packets of debris as “debritons”. The debritons represent debris flux, here defined as a volume of debris
132 transferred per model iteration per grid-cell area, [$\text{m}^3/\text{m}^2/\text{iteration}$] and are equivalent to the flow depth in the cell.
133 The present implementation of the MWR algorithm is coded in Python and developed as a component of the Landlab
134 earth surface modeling toolkit (Barnhart et al., 2020; Hobbey et al., 2017). MWR uses the Landlab raster model grid,
135 which consists of a lattice of equally sized, rectangular cells. Topographic elevation, derived topographic attributes
136 like slope and curvature, and other spatially varying attributes such as regolith depth and grain size, are recorded at
137 nodes in the center of each cell (see Figure 5 of Hobbey et al., 2017). In the subsequent sections we describe the model
138 theory. Note that all the notations of parameters and variables used in this theory are listed in Section 10.

139 **2.2 Mobilization of the initial mass wasting source material (Algorithm 1):**

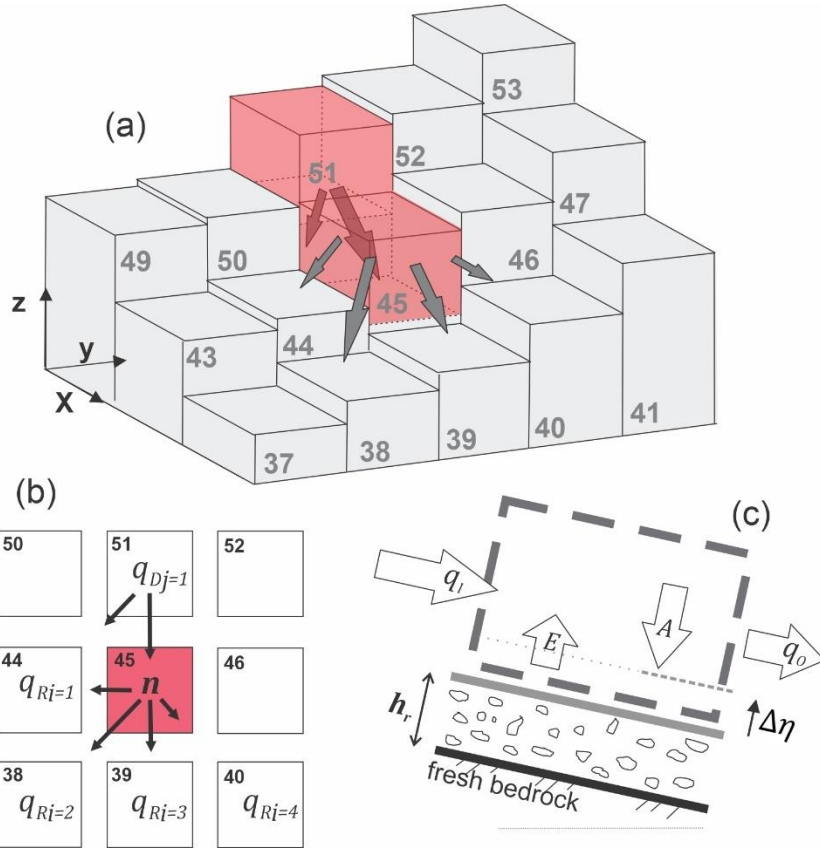
140 To initiate MWR, the user provides maps of initial topography, regolith depth, and the location and depth of the mass
141 wasting source material (e.g., landslide body). Each raster model grid node in the mass wasting source material is
142 designated as a debriton (Figure 2, iteration $t = 0$) with a magnitude equal to the mass wasting source material depth
143 and basal elevation equal to the initial topography minus the mass wasting source material depth. The basal elevation
144 can be thought to represent the rupture or slip surface of the source material and the redistribution (flux) of each
145 debriton to its downslope nodes (receiver nodes) is determined as a function of the slope of the slip surface. Note that
146 if the depth of the wasting source material is spatially variable (e.g., a rotational failure), the slope of the slip surface
147 will not match the slope of the initial terrain surface. At the lowest-elevation debriton of the source material, flux to
148 its downslope nodes is determined using the surface slope of the initial DEM (see flow direction of lowest node in
149 Figure 3a). This implementation helps to ensure that the lowest-elevation debriton in the mass wasting source material
150 moves downslope and movement of upslope debritons are impacted by the geometry of the mass wasting source
151 material. For example, the receiver nodes of the lowest-elevation debriton in the landslide illustrated in Figure 2
152 (iteration $t = 0$, detailed in Figure 3a) would be identified as those among the eight neighboring nodes whose initial
153 topographic elevation was less than the initial topographic elevation of the node while for the debriton at node 51, the

154 receiver nodes would be identified as those among the eight neighboring nodes whose topographic elevation is less
 155 than the topographic elevation of the terrain underlying the debrinton (the slip surface).



156

157 **Figure 2.** Illustration of initial mass wasting release ($t = 0$) and runoff. Notice how the list of receiver nodes changes with each
 158 iteration. The flow elongates and widens as the number of receiver nodes increase and stops when the number of receiver nodes is
 159 zero. If the incoming flux (sum of all incoming debrintons) to a node is less than q_c , the material stops, causing aggradation.



160

161 **Figure 3.** (a) Three-dimensional illustration of iteration $t = 0$ in Figure 2, showing initial source material nodes (represented by red
 162 cells) and flux towards downslope nodes. Except for the lowest elevation node in the mass wasting source material, all debris
 163 are directed downslope based on the underlying topographic slope (compare flow directions of node 51 to node 45); (b) Distribution
 164 of q_o to downslope nodes 38, 39, 40 and 44; (c) illustration of mass continuity applied to any node that receives a debris.

165

166 2.3 Flow routing and rules for debris flow erosion, deposition and resistance (Algorithm 2)

167 Algorithm 2 is essentially the runout model. It determines how each debris traverses and modifies the landscape.
 168 After receiver nodes from the first model iteration are determined in Algorithm 1 (iteration $t=0$), Algorithm 2 is
 169 repeatedly implemented until all material has deposited (i.e., there are no debris). Each debris moves one grid
 170 cell per model iteration, the larger the landslide size, the more iterations necessary to evacuate the landslide. As each
 171 debris moves, it may erode or aggrade the landscape, impacting the movement of any upslope debris. As is
 172 common with other reduced complexity models, we assume that inertial effects have negligible impact on flow
 173 behavior (i.e., the kinematic flow approximation). The downslope redistribution of a debris or flux to each of a
 174 node's i -th receiver nodes (q_{R_i}) is determined as a function of topographic slope (slope of terrain under the debris)
 175 using the Freeman (1991) multiflow direction algorithm:

$$176 \quad q_{R_i} = q_o \frac{S_i^a}{\sum_{i=1}^{NR} S_i^a} \quad (1)$$

177 where q_o is the total out-going flux from the node and has units of depth [m] per model iteration, Nr is the number
 178 of receiving nodes, i is the index for each receiver node (e.g., $i = 1, 2 \dots Nr$) and S_i is the underlying topographic
 179 slope to the i -th receiver node (Figure 3b). The Freeman (1991) multiflow direction algorithm is a commonly used
 180 approximation for two-dimensional flow, and in this implementation it is handled by a pre-existing Landlab flow-
 181 routing component. The exponent a controls how material is distributed to downslope nodes. In a braided river
 182 cellular-automaton model, Murray and Paola (1997) used an approximation for turbulent shallow water flow to justify
 183 $a = 0.5$ (which is the exponent on the slope factor in channel friction laws). For our application, we found MWR
 184 provided a closer fit to observed mass wasting runoff if $a = 1$, suggesting that the material behavior is more similar
 185 to linear-viscous shear flow than to wall-bounded turbulent shear flow. The total incoming flux (again, in units [m]
 186 per model iteration) towards a given node (q_I), is determined by summing the flux from each of the node's donor
 187 nodes:

$$188 \quad q_I = \sum_{j=1}^{Nd} q_{D_j} \quad (2)$$

189 Where Nd is the number of donor nodes, and q_{D_j} is the flux from node D_j (the j -th donor node, $j = 1, 2 \dots Nd$; Figure
 190 3b).

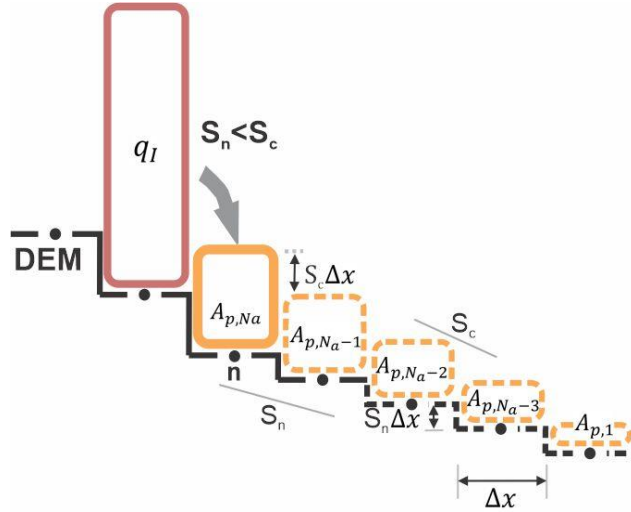
191 As noted by Tucker and Hancock (2010), the flow depths calculated from two-dimensional flow approximations like
 192 (1) can be influenced by the grid-size used to represent the terrain and depending on the boundary conditions,
 193 neglect of pressure and momentum forces may lead the model to underestimate or overestimate flow width in some
 194 circumstances. Rengers et al. (2016) noted that this same issue occurs when using a kinematic wave approximation of
 195 the shallow water equations because the kinematic wave approximation lacks a pressure term that would normally
 196 allow the modelled water surface to spread out. For the purpose of determining flow-depth-dependent erosion rates
 197 described later in this paper, and to provide a simplified representation of the effect of pressure forces, we constrain
 198 flow depths to no more than a maximum flow as:

$$199 \quad h = \min(h_{max}, q_I) \quad (3)$$

200 Where h_{max} is an effective upper limit to flow depth, that in practice can be approximated as the maximum observed
 201 flow depth, as inferred from field indicators or assigned based on expert judgement (See Section 5) and h is the
 202 corrected flow depth used to calculate flow shear stress. This correction allows erosion rates to vary with flux but
 203 prevents unreasonably large values. This flow depth correction does not violate the conservation of mass and runoff
 204 mass balance, as h is only used to calculate flow shear stress.

205 To determine aggradation (A) at a node, we use a critical slope (S_c) constraint that permits computationally-rapid
 206 distribution of q_I over multiple nodes. Critical slope constraints or rules are common to many reduced-complexity and
 207 landscape evolution models. Chen et al. (2023) showed that when flow inertia can be ignored, S_c can be approximated
 208 from the surface slope of observed deposits. Several landscape evolution models use a S_c -based nonlinear, nonlocal
 209 aggradation scheme (e.g., Campforts et al., 2020; Carretier et al., 2016) but when this rule is implemented with the
 210 debris flow framework described above, unreasonably tall deposits result when q_I is large and slope at the node (S) \ll
 211 S_c . To resolve this problem, aggradation depth can be limited to $A \leq S_c \Delta x$, (where Δx grid cell length), but we found

212 that this constraint results in long deposits that parallel the underlying slope when q_I is large. Instead, MWR computes
 213 the aggradation depth at a node assuming that the aggradation will spread over N_a nodes until all of q_I is deposited
 214 and that the surface slope of the overall deposit will be equal to S_c , as shown in Figure 4 and described as follows.



215
 216 **Figure 4.** Illustration of aggradation rule used in MWR when q_I is assumed to spread over 5 nodes ($N_a = 5$). Solid
 217 yellow box indicates deposition at node n . Dashed yellow boxes and lines indicate hypothetical deposition and
 218 underlying topography. Dots along DEM surface are nodes.

219 Aggradation at a node is determined as:

$$220 \quad A = \begin{cases} 0, & S \geq S_c \\ \min(A_{p,N_a}, q_I), & S < S_c \end{cases} \quad (4)$$

221 Where S is the steepest slope to the node's eight neighbouring nodes, A_{p,N_a} is a potential aggradation depth (A_p)
 222 necessary to form a deposit that: (1) begins at the node and spreads over N_a consecutive nodes; (2) has a total volume
 223 equal to $q_I \Delta x^2$; (3) a surface slope equal the critical slope S_c and; (4) an underlying topographic slope equal to the
 224 steepest slope at the node and assumed constant over the N_a consecutive nodes of deposition (S_n). From this assumed
 225 deposit, we can analytically define A_{p,N_a} and N_a as a function of q_I , S_c and S_n as follows:

226 First, q_I , calculated from (2), can be used to calculate $A_{p,i}$ by expressing q_I as the sum of the N_a deposits that make
 227 up the overall deposit as:

$$228 \quad q_I = \sum_{i=1}^{N_a} A_{p,i} \quad (5)$$

229 where $A_{p,i}$ is the i -th deposition amount in the deposit and $i = 1$ is the last node of deposition ($A_{p,1}$; see Figure 4).
 230 Since we assume the deposit slope and underlying topographic slope are uniform, the deposition amount at any of the
 231 N_a nodes can be determined from $A_{p,1}$ as:

$$232 \quad A_{p,i} = A_{p,1} + (i - 1)\Delta x(S_c - S_n) \quad (6)$$

233 From (6) we can re-write (5) as a function of $A_{p,1}$ and rearrange to define $A_{p,1}$ as a function of q_I :

234
$$A_{p,1} = \frac{1}{N_a} q_I - \frac{N_a - 1}{2} \Delta x (S_c - S_n) \quad (7)$$

235 Substituting (7) into (6) and solving for $i = N_a$, we get an expression for A_{p,N_a} :

236
$$A_{p,N_a} = \frac{1}{N_a} q_I + \frac{N_a - 1}{2} \Delta x (S_c - S_n) \quad (8)$$

237 Equation (8) can be rearranged into a quadratic equation and solved for N_a as:

238
$$N_a = \frac{-A_{p,1} + \frac{1}{2} \Delta x (S_c - S_n) \pm \sqrt{\left(A_{p,1} - \frac{1}{2} \Delta x (S_c - S_n) \right)^2 + 2 \Delta x (S_c - S_n) q_I}}{\Delta x (S_c - S_n)} \quad (9)$$

239 We use (8) to solve for A_{p,N_a} and (9) to solve for N_a assuming $A_{p,1} = 1/2 \Delta x S_c$ and rounding the positive solution to
 240 the nearest integer. When implemented using a single debriton, released on a two-dimensional hillslope as illustrated
 241 in Figure 4, the debriton deposits over N_a nodes at a uniform slope equal to S_c . When implemented on an actual three-
 242 dimensional terrain, the interaction between multiple debritons in multiple directions creates a complex deposit whose
 243 slope changes with S_c .

244 To determine erosion depth (E) [m/iteration], we constrain E to the lesser of a potential erosion depth, h_e , and local
 245 regolith depth, h_r :

246
$$E = \min (h_r, h_e) \quad (10)$$

247 where h_e is computed as a function of the basal shear stress of the flow, τ [Pa], (Equations 12 and 13) and the critical
 248 shear stress (τ_c) of the regolith at the node [Pa]:

249
$$h_e = k(\tau - \tau_c)^f \quad (11)$$

250 The coefficient k is an erodibility parameter [m/Pa^f]. Stock and Dietrich (2006) showed that k encapsulates substrate
 251 properties. If h_e is used to represent erosion over geomorphic time scales, with repeated debris flow occurrences in a
 252 single model iteration, k becomes associated with debris flow length and frequency (Perron, 2017). In our application
 253 since we are modelling the erosion associated with a single runout event, as represented by the downslope movement
 254 of the debritons, the coefficient k therefore needs to scale h_e on the order of the average erosion depth caused by a
 255 single debriton. Using this logic, k can be computed using the observed average erosion depth and an estimated length
 256 of the runout material that caused the erosion. Further details on how we determine k from observed runout are
 257 included in the Supplementary Material. The exponent f controls the non-linearity of h_e . Many authors (Chen &
 258 Zhang, 2015; Frank et al., 2015; Shen et al., 2020) use a value of 1 for f but field measurements by Schürch et al.
 259 (2011) (see their Figure 3) suggest that f may be less than 1 if τ is assumed to vary linearly with flow depth,
 260 particularly at flow depths greater than 3 meters.

261 MWR includes two options for defining τ : (1) a quasi-static basal shear stress approximation or (2) a grain-size-based
 262 shear stress approximation. The quasi-static basal shear stress approximation (e.g., Takahashi, 2014) is defined as:

263
$$\tau = \rho g h \sin \theta \quad (12)$$

264 where ρ is the density of mass wasting material (grain and water mixture) [kg/m³], g is gravity [m/s²] and h is the
 265 adjusted flow depth described in (3) and θ is the topographic slope ($\tan^{-1}(S)$) measured in degrees.

266 The grain-size-based shear stress approximation is defined using an empirical formula by Bagnold (1954):

$$267 \quad \tau = \sigma \tan \varphi \quad (13)$$

268 Where σ is normal stress [Pa], φ is the collision angle between grains, measured from the vertical axis (See Bagnold,
 269 1954), with a value of $\tan \varphi$ typically equal to 0.32. Stock and Dietrich (2006) defined σ as:

$$270 \quad \sigma = \cos \theta v_s \rho_s D_s^2 \left(\frac{du}{dz} \right)^2 \quad (14)$$

271 Where v_s is the volumetric solids concentration, ρ_s is density of the solids [kg/m³], u is flow velocity [m/s], z is depth
 272 below the flow surface [m], du/dz is the shear strain rate [1/s] and D_s is the representative grain size [m]. Stock and
 273 Dietrich (2006) suggested that D_s corresponds to a small percentile of the coarsest fraction of the runout material (D_{88}
 274 to D_{96}) and they approximated du/dz as:

$$275 \quad \frac{du}{dz} = \frac{u}{h} \quad (15)$$

276 Solely for the purpose of computing du/dz , we approximate velocity at a node using a grain-size dependent empirical
 277 formula for debris flow velocity by Julien and Paris (2010) as:

$$278 \quad u = 5.75 u^* \log \left(\frac{h}{D_s} \right) \quad (16)$$

279 Where u^* is shear velocity ($\sqrt{gh \tan \theta}$). Substituting (16), (15), (14) and (13) into (11) yields a grain-size dependent
 280 approximation for h_e that mimics the non-linear erosion response to flow depth in Schürch et al. (2011). Additionally,
 281 this form of τ is advantageous because it permits landslide-driven erosion rates to scale with landslide grain size,
 282 which can vary by lithologic region (e.g., Roda-Boluda et al. 2018). As will be shown in Section 5, we obtained
 283 reasonable model calibration at multiple sites by defining D_s from the coarser grain sizes observed in the field at
 284 existing runout-deposits, road-cuts and tree-throw pits.

285 Once A [m] and E [m] have been determined, total out-going flux per iteration, q_o [m] is determined as (see Figure
 286 3c):

$$287 \quad q_o = \begin{cases} q_I - A + E, & q_I \geq q_c \\ 0, & q_I < q_c \end{cases} \quad (17)$$

288 Where q_c is a threshold flux for deposition. When $q_I < q_c$, q_I deposits and q_o becomes zero. The threshold flux q_c
 289 conceptually represents the flow depth below which flow resistance is large enough to cease the forward momentum
 290 of the flow, whether in the form of internal friction or friction due to vegetation and obstructions (e.g., large clasts or
 291 logs). The density and water content of q_I , A , and E are treated as uniform and surface runoff, such as channelized
 292 stream flow or hillslope-infiltration-excess runoff, that might mix with q_I . A , or E is ignored. Once q_I , A , q_o and E
 293 have been determined, change in elevation at a node ($\Delta\eta$) is calculated as:

$$294 \quad \Delta\eta = A - E \quad (18)$$

295 Attributes of the debriton and regolith are updated using a volumetric-weighted average approach. First, for each
 296 regolith attribute being tracked by the model (e.g., grain size), the attribute value delivered to a node from its donor
 297 nodes (ξ_D) is determined as:

$$298 \quad \xi_D = \frac{\xi_D \cdot \mathbf{q}_D}{q_I} \quad (19)$$

299 where \mathbf{q}_D is a vector containing all q_{D_j} sent to the node, ξ_D is a vector containing the incoming attribute values for
 300 each q_{D_j} , and q_I is the sum of incoming flux from donor nodes defined by (2).

301 Second, the attribute value sent from a node to its receiver nodes (ξ_R) is determined as:

$$302 \quad \xi_R = \frac{\xi_{t-1}E + \xi_D(q_I - A)}{q_O} \quad (20)$$

303 where ξ_{t-1} is the attribute value at the node before any aggradation (i.e., the previous iteration attribute value). Finally,
 304 the attribute value at the node, updated to account for erosion and aggradation (ξ) is:

$$305 \quad \xi = \frac{\xi_{t-1}(h_r - E) + \xi_D A}{A + h_r - E} \quad (21)$$

306 Regolith thickness (h_r) and topographic elevation (η) are updated at a node as:

$$307 \quad \eta = \eta_{t-1} + \Delta\eta \quad (22)$$

$$308 \quad h_r = h_{r,t-1} + \Delta\eta \quad (23)$$

309 Where η_{t-1} and $h_{r,t-1}$ are the topographic surface elevation and regolith thickness at the node from the previous
 310 model iteration. After regolith thickness and topographic elevation have been updated for each debriton, the multi-
 311 direction slope of the DEM, which is used for routing the debritons in the next model iteration, is recomputed from
 312 the topographic surface.

313 Using the above approach, debritons may become obstructed if they encounter a topographic pit or flat topography in
 314 the DEM. To allow a debriton to pass an obstruction, we rely on a simple work-around: upon encountering the
 315 obstruction, the debriton is directed to itself and some portion of the debris is deposited based on (4). At the end of
 316 the model iteration, the node elevation and slope are updated. During the next iteration, if the remaining mobile debris
 317 is no longer obstructed, it moves to its downslope node(s). If the node is still obstructed, it is again sent to itself until
 318 either all material has deposited or the elevation of the node exceeds that of its neighbour nodes, allowing the debriton
 319 to move downslope.

320 **3. Calibration and MWR probability**

321 **3.1 Calibration utility**

322 MWR includes an adaptive Markov Chain Monte Carlo (MCMC) calibration algorithm described by Coz et al. (2014)
 323 and Renard et al. (2006). The user provides an initial (prior) guess of the parameter values and their respective
 324 probability distribution functions (PDF) that calibrate the model to a specific site. Then, the calibration algorithm
 325 randomly selects a set of parameter values (Λ) from the prior PDFs and runs MWR using Λ . Once the model has

326 completed the run, the algorithm evaluates the posterior likelihood of the parameter set ($L(\Lambda)$) as a lumped index of
 327 model ability to replicate observed runout (described below) and the prior likelihood of the parameter set. After the
 328 first $L(\Lambda)$ has been determined, the algorithm selects a new set of parameters (Λ_{t+1}) by jumping some distance from
 329 each parameter in Λ space. Depending on the value of $L(\Lambda_{t+1})$, the algorithm either stays at Λ or moves to Λ_{t+1} . This
 330 Markov process is repeated a user-specified Nc times. Jump direction is random, but the algorithm is adaptive because
 331 the jump distance changes depending on how often $L(\Lambda_{t+1}) > L(\Lambda)$. For a detailed description of the algorithm see
 332 Coz et al. (2014).

333 The $L(\Lambda)$ index is estimated as the product of the prior probability of the selected parameter values, $p(\Lambda)$, and three
 334 other performance metrics as:

$$335 \quad L(\Lambda) = p(\Lambda) * \Omega_T * \frac{1}{\Delta\eta_E^2} * \frac{1}{Q_{sE}^2} \quad (24)$$

336 where Ω_T is the Lee-Salle index (Heiser et al., 2017) for model planimetric fit; and $\Delta\eta_E$ and Q_{sE} are new
 337 dimensionless indices, proposed for this study. The indice $\Delta\eta_E$ is the volumetric error of the modelled topographic
 338 change normalized by the observed total mobilized volume (initial landslide + erosion volume). The indice Q_{sE} is the
 339 mean-cumulative flow error along the modelled runout path normalized by the observed mean cumulative flow. Larger
 340 values of Ω_T and smaller values of $\Delta\eta_E$ and Q_{sE} indicate modelled runout more closely fits observed. Note that we
 341 add a value of 1 to Ω_T and use the squared- reciprocal values of $\Delta\eta_E$ and Q_{sE} in (24) so that the magnitude of $L(\Lambda)$ is
 342 always equal to or greater than zero and increases with improved fit. The metric Ω_T is written as:

$$343 \quad \Omega_T = \frac{\alpha - \beta - \gamma}{\alpha + \beta + \gamma} + 1 \quad (25)$$

344 where α, β and γ are the areas of matching, overestimated and underestimated runout extent, respectively.

345 The spatial index for volumetric error, $\Delta\eta_E$, is determined as:

$$346 \quad \Delta\eta_E = \sqrt{\frac{\sum_{i=0}^p [(\Delta\eta_{oi} - \Delta\eta_{mi}) \Delta x^2]^2}{V^2}}. \quad (26)$$

347 Where V is observed total mobilized volume and p is the number of nodes in the modelled runout extent, and $\Delta\eta_{mi}$
 348 and $\Delta\eta_{oi}$ are the modelled and observed topographic change [m] at the i -th node within the runout extent.

349 To calculate Q_{sE} , we first determine the cumulative debris flow volume (Q_s) at each node, j , ($Q_{s j}$) along the runout
 350 profile, in a manner similar to the flow volume/mass balance curves in Fannin and Wise (2001) and Hungr and Evans
 351 (2004):

$$352 \quad Q_{s j} = -\Delta x^2 \sum_{i=1}^{u_j} \Delta\eta_{i,j} \quad (28)$$

353 where $\Delta\eta_{ij}$ is the topographic change [m] at the i -th node located upstream of node j , and u_j is the total number of all
 354 nodes located upstream of j . $Q_{s j}$ is computed for both the observed and modelled runout ($Q_{so j}$ and $Q_{sm j}$
 355 respectively) and Q_{sE} of a runout is determined as:

$$Q_{sE} = \sqrt{\frac{\frac{1}{r} \sum_{j=1}^r (Q_{sOj} - Q_{sMj})^2}{Q_{sO}^2}} \quad (29)$$

Where r is the number of nodes along the runout profile, and $\overline{Q_{sO}}$ is the observed mean cumulative flow. As will be detailed in Section 5, field estimates for S_c and q_c , vary over the length of the runout path. To account for the heterogeneity of S_c and q_c , we estimate prior distributions of potential S_c and q_c values from field/remote sensing measurements. Then, from model calibration to a DEM-of-Difference (pre-runout DEM subtracted from the post-runout DEM; DoD using the calibration utility, we find single values of S_c and q_c that allow the modelled DoD to replicate the observed DoD .

We run the calibration utility using a single Markov chain of 2000 repetitions. At most sites, the model converged relatively quickly on a solution and we therefore didn't consider burn-in or evaluate convergence (e.g., Gelman et al. 2021). Future implementations of the calibration utility may include multiple chains, burn-in and a check for convergence. As a final note, many debris flow runout models are evaluated using Ω_T or variations of Ω_T alone (e.g., Gorr et al., 2022; Han et al., 2017) and the MWR calibration utility can also be run solely as a function of Ω_T . However, we found that calibration based on Ω_T alone results in high parameter equifinality (e.g., Beven 2006); multiple parameter sets result in an equally calibrated model as evaluated by Ω_T . As such, we recommend calibrating debris flow models to an observed DoD. If repeat lidar is available, a DoD can be obtained from before and after scans of the observed runout event. Alternatively, a DoD can be created by hiking the observed runout event and mapping field-interpreted erosion and deposition depths. Additional details on how we prepared DoDs for multiple sites are included in the Supplementary Material.

374
375

3.2 Mapping landslide runout hazard

MWR includes an additional utility called MWR Probability that produces landslide runout probability maps. MWR Probability repeatedly runs MWR a user specified Np times, each repetition with a different, randomly sampled parameter set from the posterior parameter PDFs produced by the calibration utility. MWR Probability includes three options for specifying the initial mass wasting source material: (1) a user-provided landslide source area polygon(s) based on field and/or remote sensing observations; (2) a user-defined hillslope susceptible to landslides (e.g., potentially unstable slope), where landslide area and location are randomly selected within, but no larger than the hillslope; this option is useful when the extent of a potential landslide is unknown; and (3) a series of mapped landslide source areas within a watershed, as determined by an externally run Monte Carlo landslide initiation model (e.g., Hammond et al. 1992; Strauch et al., 2018) ; this option is useful for regional runout hazard applications. If using Option 1, modelled runout probability represents uncertainty in MWR parameterization. If using Option 2 or 3, modelled runout probability reflects uncertainty in both MWR parameterization and landslide location and size.

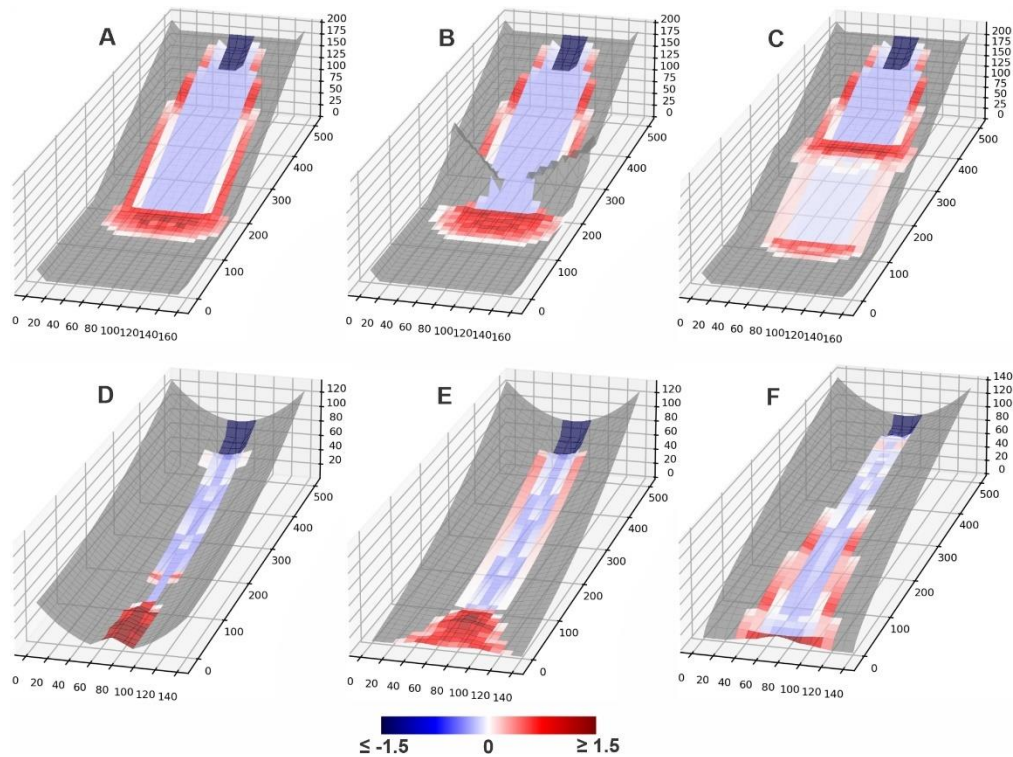
388 For all three run options, each model iteration begins with the same initial topography. After Np model simulations,
 389 Np different versions of the post-runout landscape are created, and model performance for each are evaluated. After
 390 Np model runs, probability of runout at each model node is determined as:

$$391 \quad P(\Delta\eta) = \frac{\text{number_of}(|\Delta\eta|>0)}{Np} \quad (30)$$

392 where $\text{number_of}(|\Delta\eta| > 0)$ is the number of times topographic elevation at a node changes as a result of erosion
 393 or deposition from the Np model runs. Probability of erosion or aggradation can be determined by replacing the
 394 numerator in (30) with $\text{number_of}(\Delta\eta < 0)$ or $\text{number_of}(\Delta\eta > 0)$ respectively.

395 4. Basic model behavior

396 We evaluate basic model behavior using a series of virtual experiments. The virtual experiments consist of six
 397 synthetic terrains including: (A) a planar slope that intersects a gently sloped plane ($S = 0.001$), (B) a planer slope
 398 with a constriction, that intersects a gently-sloped plane, (C) a planar slope that has a bench mid-slope and then
 399 intersects a gently-sloped plane; (D) a concave up, uniform-convergence slope; (E) a concave up, variable-
 400 convergence slope that widens (convergence decreases) in the downslope direction; (F) a convex up, variable-
 401 convergence slope that widens (convergence decreases) in the downslope direction. On each terrain, a 30-meter wide,
 402 50-meter long and 3-meter deep landslide is released from the top of the terrain. All six terrains are covered by a 1-
 403 meter thick regolith and use the same parameter values ($S_c = 0.03$, $q_c = 0.2$ m, $k = 0.01$, $D_p = 0.2$ m). Experiment
 404 results are shown in Figure 5.



405

406 **Figure 5.** Shaded, 3-D visualizations of model response to six different synthetic terrains, colored according to the
407 DoD of the final runout surface. Red indicates a positive change in the elevation of the terrain (aggradation) and
408 blue indicates a negative change (erosion). Grid size is 10 meters. 3-D representation of DoD is exaggerated by a
409 factor of 5 to make visible in figure.

410 On Terrain A, the landslide spread as it moved downslope and formed levees along the edge of the runout path. The
411 width of the spread was a function of the multiflow direction algorithm and resistance along lateral margins of the
412 runout as represented by q_c . At the slope break at the base of the slope, the material deposited at an angle controlled
413 by S_c . On Terrain B, the flow initially eroded and deposited identical to the first but near the slope break, the
414 topographic constriction forced flow depth to increase and exceed q_c , minimizing the formation of levees (because
415 $q_0 > q_c$) and resulted in a slightly larger deposit at the base of the slope. On Terrain C, landslide runout was again
416 initially identical to the runout on Terrain A; however, upon intersecting the mid-slope bench, most of the runout
417 material deposited. A small, thinner portion did continue past the bench but eroded at a lower rate than the initial slide
418 upslope of the bench. Upon intersecting the flat surface at the base of the hillslope, the runout material deposited.

419 On Terrain D, the landslide and its runout were confined to the center of convergent terrain and only deposited once
420 the slope was less than S_c . The slide never widened because the uniformly convergent channel shape prevented
421 spreading and the narrower flow width maintained a higher flow depth, which prevented the formation of levees. On
422 Terrain E, the landslide again deposited once slope was less than S_c but because topographic convergence of Terrain
423 E decreases in the downslope direction, as the runout material moved downslope, the deposit spread more than on
424 Terrain D, which caused thinner flow and deposition along margins of the runout path. On the final terrain, Terrain F,
425 slope is always greater than S_c so deposition was limited to levees along the edge of the flow that formed as the runout
426 spread in response to decreasing convergence.

427 MWR model behavior can be summarized as follows. The displacement and deposition of landslide material predicted
428 by MWR responds to topography in a reasonable manner: Flow width increases as convergence decreases (e.g, Terrain
429 F), which in turn reduces flow depth. Lower flow depths cause lower erosion rates and reduce aggradation extent.
430 Conversely, modelled flow depth increases when convergence increases (e.g., Terrain B). Where the flow encounters
431 broadly convergent or planer slopes, lateral levee deposits form, a common feature of landslides reported in the
432 literature and at sites reported here (see Section 5) that detailed mechanistic models can struggle to reproduce (e.g.,
433 Barnhart et al, 2021).

434 We did not attempt to compare MWR modelled flow with the output of shallow-water-equation based models or
435 observed granular flows (e.g., Medina et al, 2008; McDougall and Hungr, 2004; Iverson and Denlinger, 2001; Han
436 et al., 2015). The cellular automaton representation in MWR does not model the time-dependent evolution of debris
437 flow velocity and depth, and conceptually moves debris instantaneously at each iteration, as driven by changes in the
438 evolving topographic elevation field. Because of that, only the final outcome of MWR can be compared with other
439 models or observed runout, which we do in the next section.

440 **5. Model Validation:**

441 **5.1 Overview**

442 In this section, we demonstrate the ability of a calibrated MWR to replicate observed runout extent, sediment transport
 443 and topographic change at field sites located in the western USA and summarize model calibration results with an
 444 evaluation of MWR calibration relative to terrain attributes of the observed runout paths. Note that simply calibrating
 445 a model to match field data does not constitute a satisfactory test of model predictive ability (Iverson, 2003). Strategic
 446 testing, which involves calibrating the model to one site or period of time and then running the calibrated model at a
 447 separate site or period of time (Murray, 2013), is a better indicator. Two of our validation sites, the Cascade Mountain
 448 and Olympic Mountain sites, include two separate landslides and subsequent runout and we test model predictive
 449 ability at these sites in Section 6.

450 Calibrated model performance is demonstrated at the following field sites (see Figure 6a for locations and observed
 451 runout extent): (1) two runout events over the same hillslope in the Cascade Mountains (Washington state [WA],
 452 USA): a large debris avalanche in 2009 (Cascade Mountains, 2009) and a moderately-sized debris flow in 2022
 453 (Cascade Mountains, 2022) that inundated and flowed within a first-to-second order channel until perpendicularly
 454 intersecting a narrow river valley several hundred meters below the landslide (Figure 1a); (2) debris flows in the Black
 455 Hills (WA) sourced from a small failure along the toe of a deep-seated landslide (Black Hills, South) and a moderately-
 456 sized debris avalanche from a large road fill (Black Hills, North) that flowed several kilometers along a relatively
 457 wide, broadly convergent channel before stopping (Figure 1b); (3) a single, moderately-sized debris avalanche in the
 458 Rocky Mountains (Rocky Mountains), the majority of which flowed several hundred meters over a broadly convergent
 459 to divergent hillslope in Colorado (Figure 1c); and (4) a 30-year chronology of small landslides and subsequent debris
 460 flows in the Olympic Mountains (WA) in steep, highly convergent channels that flowed well over a kilometer and
 461 coalesced into a single runout deposit in a dendritic, channelized watershed (Olympic Mountains; Figure 1d). All
 462 landslides initiated during heavy rainfall or rain-plus-snowmelt storm events (WRCC, 2022; NRCS, 2022; Table 1)
 463 but their runout varied in terms of erosion rate, grain size (Figure 6b), depositional behavior (Figure 6c) and the
 464 topographic convergence of the underlying terrain.

465 **Table 1.** Landslide and runout characteristics

site	Cascade Mountains, 09	Cascade Mountains, 22	Black Hills, south	Black Hills, north	Rocky Mountains	Olympic Mountains
landslide length, ℓ [m]	185	55	80	75	40	45
landslide width [m]	80	50	15	65	35	15
landslide volume [m ³]	110,000	22,000	1,500	18,500	4,600	400 - 2,200
2-day cumulative precipitation + snowmelt [mm]	120+85	140+75	205+50	205+50	193+0	100 - 220 + ?
maximum grain size [m]	0.316	0.316	0.48	0.206	0.984	0.8
Slope range of positive-net deposition [%]	1 - 15	1 - 15	<1 - 10	<1 - 8	16 - 25	5 - 15
average flow depth in scour zone [m] ^a	4	2	2	3	3	3
average channel slope in scour zone [m/m]	0.25	0.25	0.15	0.15	0.4	0.3

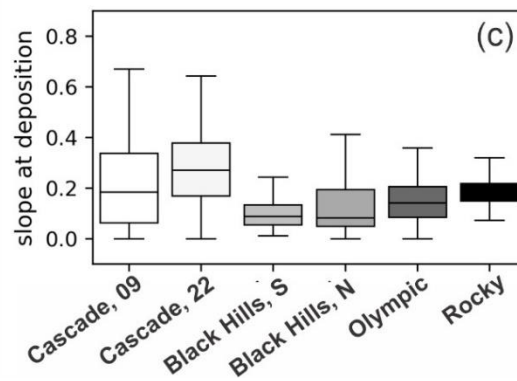
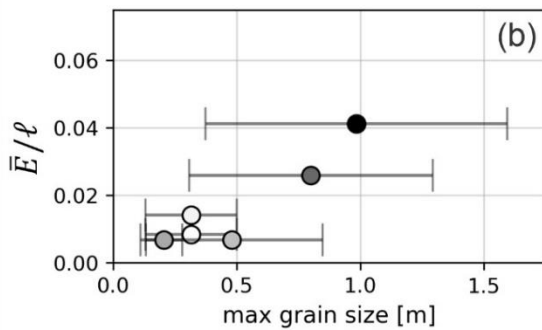
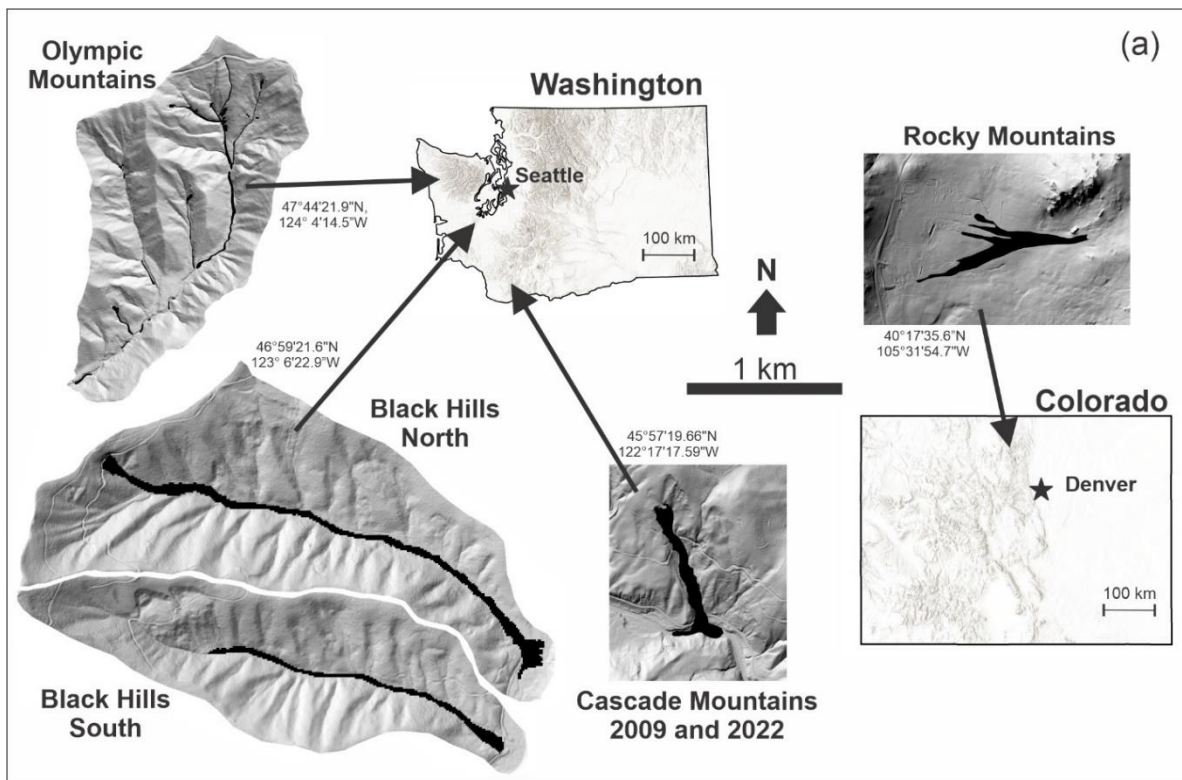
average channel width in scour zone [m]	45	20	25	35	55	10
length of erosion, [m]	600	340	1210	1345	360	2550
erosion area, A [m ²]	28,400	6,600	22,800	52,400	20,800	28,900
erosion volume, $\sum E\Delta x^2$ [m ³] ^b	44,547	5,125	12,332	26,815	34,275	33,725
average erosion per unit length of landslide, \bar{E}/ℓ , [m/m]	0.0085	0.014	0.0068	0.0068	0.041	0.026
k	0.020	0.034	0.017	0.020	0.076	0.051
growth factor, [m ³ /m]	74.2	15.1	10.2	19.9	95.2	13.2
average observed $ \Delta\eta $ [m]	2.4	2.2	0.53	0.63	0.89	1.4
total erosion volume / total mobilized volume ^c	0.29	0.19	0.89	0.59	0.88	0.97

466 ^a rough approximation based on landslide volume, channel width and height of scour marks in erosion zone

467 ^b excludes landslide volume

468 ^c total mobilized volume = erosion volume + landslide volume

469



470

471 **Figure 6 (a)** Landslide locations in Washington and Colorado states. Coordinates next to each site are WGS84.
472 Shaded DEMs of each site are shown at the same scale. **(b)** Observed average erosion rate per unit landslide length
473 (\bar{E}/ℓ) relative to the observed average-maximum grainsize. Error bars indicate standard deviation. **(c)** Underlying
474 topographic slope of observed deposition locations.

475 **5.2 Model setup and field parameterization**

476 Each model was set up on a 10-meter grid representation of the pre-event DEM. The extent of the mass wasting source
477 material, which in all cases was a landslide, was interpreted from a combination of lidar, air-photo and field
478 observations. At all locations, we use (13) to approximate shear stress. We field-surveyed each site, noting the
479 maximum flow thickness, typical deposition and erosion depths and the size of the largest grains in the runout deposits.
480 We estimated parameter values from these field and remote observations (See Table 1). A site-specific value for k
481 was determined as a function of the observed average erosion depth (determined as total erosion volume divided by
482 the erosion area, \bar{E}) relative to the landslide length (ℓ). Further details are described in the Supplementary Material.
483 The initial mass wasting source material (e.g., the initial landslide body) ranged in volume from 400 to 110,000 m³
484 across sites. At all sites, erosion and subsequent entrainment added to the total mobilized volume (initial landslide +
485 erosion volume), but the contribution was highly variable. The erosion volume divided by the total mobilized volume
486 was as low as 0.19 at the Cascade Mountain, 2022 landslide to as high as 0.97 at the Olympic Mountain landslides
487 (Table 1).

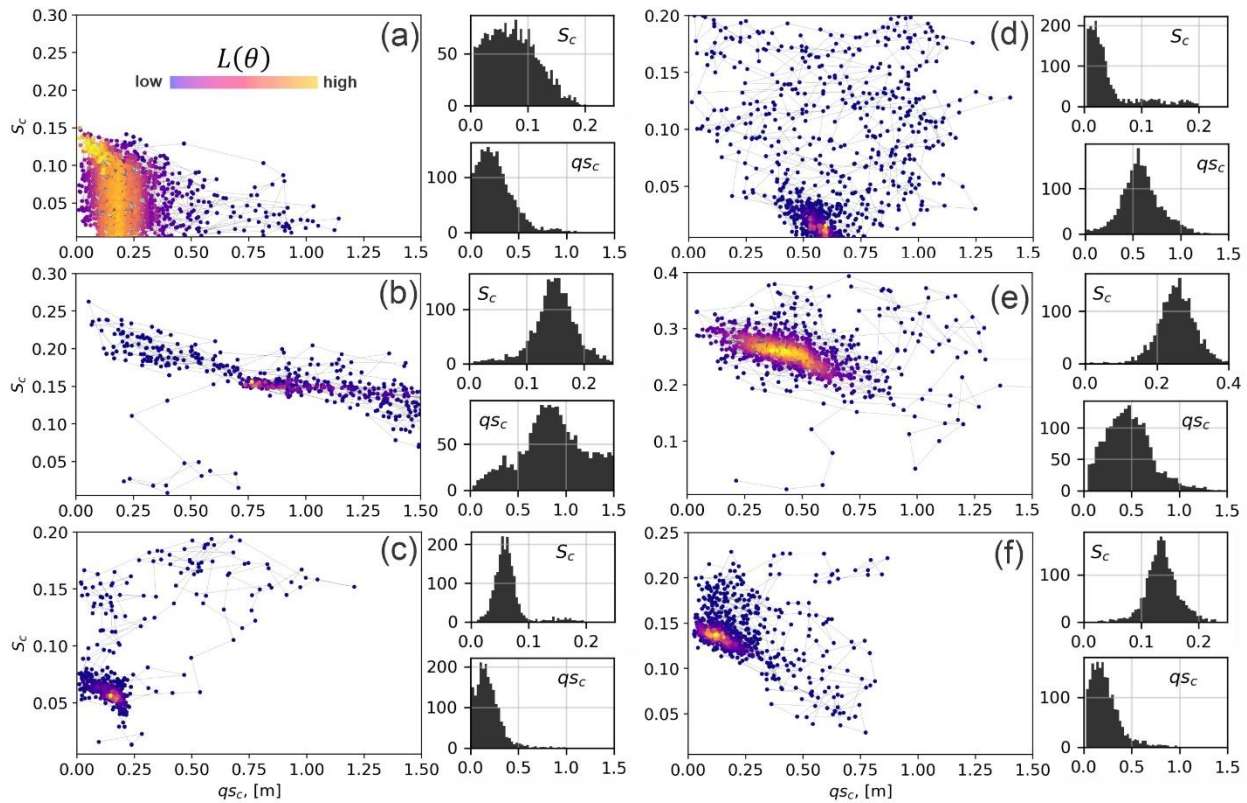
488 The average maximum grain size varied from 0.2 m at the Black hills sites to nearly 1 m at the Rocky Mountain Site
489 (Figure 6b, Table 1). Values of \bar{E}/ℓ ranged from 0.007 to 0.041 [m/m] with the highest rate occurring at the Rocky
490 Mountain landslide and the lowest at the Black Hills sites. In terms of growth factors (average volumetric erosion per
491 unit length of the erosion-dominated region of the runout path, Hungr et al. 1984; Reid et al., 2016) values ranged
492 from 10 m³/m at the Black Hills South site to 95 m³/m during the Rocky Mountain landslide (Table 1).

493 The median values of topographic slopes at which observed deposition occurred (i.e., $\Delta\eta > 0$) ranged between 0.3
494 and 0.1 across sites, while deposition was also observed in much steeper (>0.4) slopes, and much flatter slopes at some
495 sites (Figure 6c) (Table 1). The slope of channel reaches where net deposition (cumulative erosion and deposition;
496 e.g., Guthrie et al., 2010) was positive tended to be lowest at the Black Hills site (<1% to 10%) and highest at Rocky
497 Mountain site (16% to 25%).

498 We defined uniform prior distributions of S_c and q_c based on the field observations and then used the calibration utility
499 to find the best-fit parameter values (parameter values corresponding to the highest $L(\Lambda)$). Minimum and maximum
500 values of S_c were initially estimated from the range of observed slope of areas of positive-net deposition (Table 1).
501 Minimum and maximum values of q_c were set as 0.01 to 1.75, which roughly represents the range of minimum
502 observed thickness of debris flow termini in the field at all of the validation sites. For the purpose of implementing
503 the calibration utility, we prepared a DoD of each site. The DoD was determined either from repeat lidar or field
504 observations as detailed in the Supplementary Material.

505 5.3 Calibration and model performance

506 Markov chains, colored according to the likelihood index, $L(\Lambda)$ are plotted in the S_c - q_c domain, along with
 507 histograms of sampled S_c and q_c values for each landslide in Figure 7. Each Markov chain includes 2000 model
 508 iterations. The runtime for 2000 model iterations depended on model domain and landslide size but varied from
 509 roughly 1.5 to 6 hours on a 2016 2.1 GHz Intel Core Xeon, 32 GB memory desktop. The chains show a wide array
 510 of sampling patterns and parameter ranges but broadly speaking, at all sites, the algorithm jumped within S_c - q_c space
 511 towards higher $L(\Lambda)$, to form bell-shaped posterior distributions for each parameter. Depending on the landslide type,
 512 the calibration algorithm converged on different S_c - q_c pairs. For example, at the Cascade Mountains site, the
 513 calibration utility converged to smaller q_c and S_c values for the 2009 event (Figure 7a), which permitted thinner flows
 514 over lower slopes and effectively made the 2009 modelled runout more mobile relative to the 2022 modelled runout
 515 (Figure 7b). At the Rocky Mountains site, a relatively high q_c value helps control lateral extent of the modelled runout
 516 that in the field was controlled by standing trees (Figure 7e).



517 **Figure 7.** MWR calibration results for (a) Cascade Mountains, 2009; (b) Cascade Mountains, 2022, (c) Black Hills,
 518 South; (d) Black Hills, North; (e) Rocky Mountains and; (f) Olympic Mountains. Each result shows a scatter plot of
 519 the sampled S_c and q_c values, colored by their relative $L(\Lambda)$ value. To the right of each scatter plot are histograms of
 520 the iterated S_c and q_c parameters, which represent an empirical PDF of the possible S_c and q_c values that calibrate
 521 MWR to the site. Note y-axis scale differs between plots.
 522

523
 524 Profile plots of modelled Q_s and maps of the modelled planimetric runout extent, colored to indicate where the runout
 525 matched (α), overestimated (β) or underestimated (γ) the observed runout are shown in Figure 8. Values of Ω_T we

526 obtained with MWR are comparable or higher than reported values of Ω_T in the literature that used a variety of models
527 (Gorr et al., 2022; Barnhart et al., 2021; Note, to compare Ω_T values to those studies, subtract 1 from values reported
528 in this study). Across the sites, the volumetric error of the model, $\Delta\eta_E$, ranges between 6% and 15% (median 9.1%)
529 of the total mobilized volume from the observed DoD. An overall <10% volumetric error is reasonable considering
530 the low number of parameters required to calibrate MWR and that empirical estimates of total mobilized volume used
531 to run other runout models can vary by as much of an order of magnitude (e.g., Gartner et al., 2014; Barnhart et al.,
532 2021). Model performance in predicting volume flux along the runout profile was within similar error ranges. Except
533 for the Rocky Mountains site where MWR consistently modelled wider-than-observed flow, the cumulative flow error
534 along the runout profile (Q_{sE}) were limited to 5%-19% of the mean cumulative flow determined from the observed
535 DoD.

536 MWR generally successfully replicates observed sediment transport along the runout path via model parameterizations
537 that are unique to each landslide. For example, the profile plots of Q_s at the Cascade Mountain site (Figure 8a and 8b)
538 show that during the 2009 landslide, all of the runout material flowed past the first 750 meters of the runout path.
539 During the 2022 landslide, material began to deposit just down slope of the initial landslide scar, as both observed and
540 modelled Q_s reverse slope, indicating loss in downstream volume flux. Model comparisons in the Cascade Mountains
541 site were limited to the upper 750 m of the hillslope because a large portion of the runout material was lost to fluvial
542 erosion in the valley (see Supplementary Material).

543 MWR also successfully replicates the observed sediment transport patterns at the Olympic Mountains site (profile plot
544 of Q_s in Figure 8f) and to a lesser degree, the Rocky Mountain site (Figure 8e). This finding is notable, because at the
545 Olympic Mountain site, observed runout extent and sediment depositional pattern were heavily impacted by woody
546 debris. Similarly, at the Rocky Mountains site, the width of the runout appeared to be restricted by trees. (See
547 Supplementary Material).

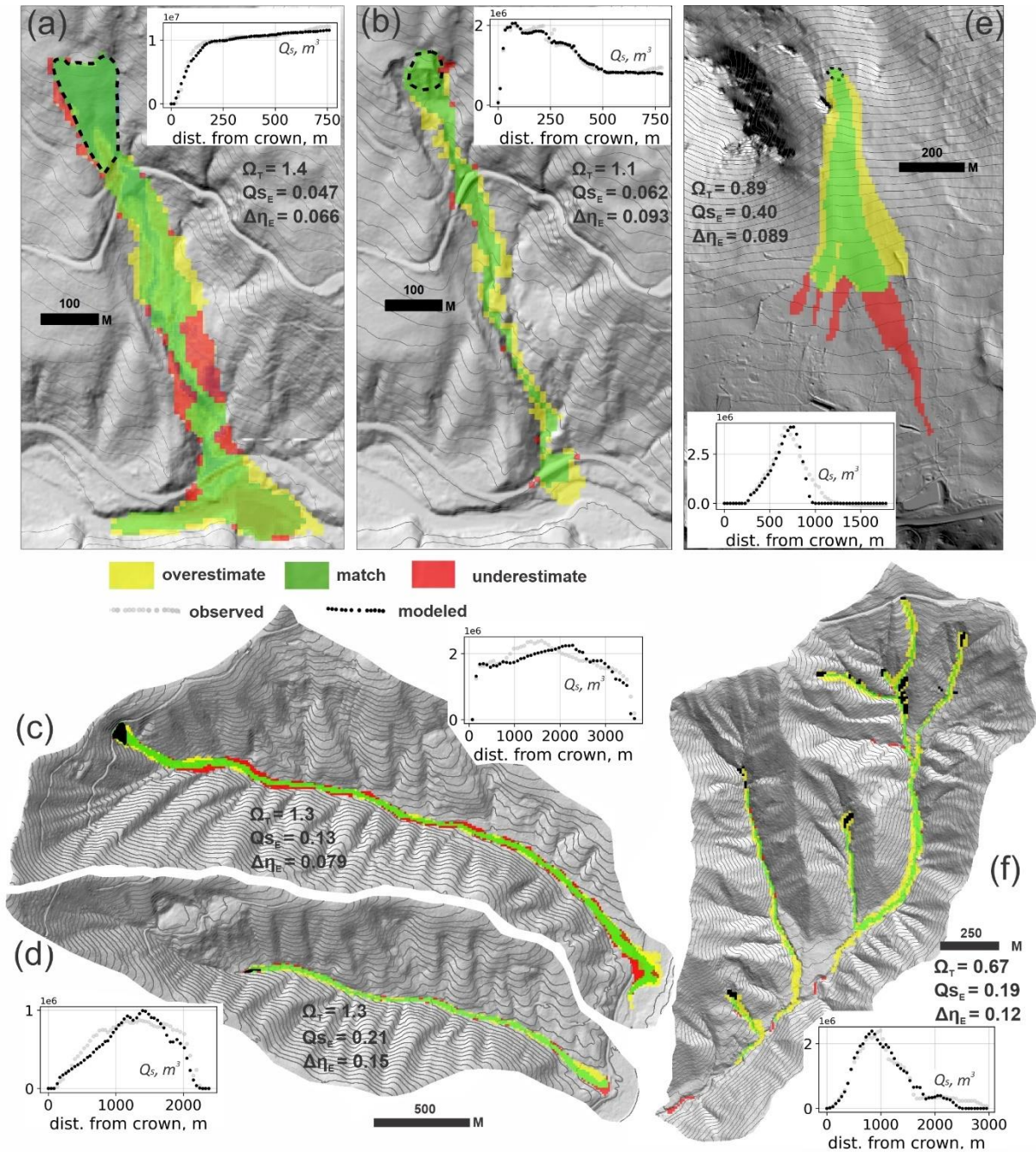
548 Using a fixed cell size of 10-m might have impacted model performance in some areas. MWR tended to over-estimate
549 the runout width for small landslides like the Olympic Mountains and Cascade Mountains, 2022 sites (yellow zones
550 in Figures 8f and 8b), likely because of the 10-m grid size used to represent the terrain. A 10-m DEM is generally
551 accepted as a good balance between model detail and computational limitations (e.g., Horton et al. 2013). However,
552 for small landslides, the 10-m grid is close to the size of the channels that controlled observed runout (Supplementary
553 Material) and may not have accurately represented the terrain. Modelled flow was less topographically-constrained
554 and tended to flow over a wider area of the terrain than observed in the more confined and smaller channels within
555 the axis of the runout valleys.

556 Because MWR does not have an explicit representation of flow momentum, it may show poor performance in regions
557 of the runout path where momentum controls runout extent. For example, at the Cascade Mountain, 2009 slide,
558 modelled extent misses a bench located along the east edge of the runout path (large red zone in Figure 8a). Review
559 of model behavior for this slide (Figure 9) shows how MWR successfully mimics diverging flow around a broad ridge
560 in the middle of the runout path (iteration $t=28$ in Figure 9), but afterward converges too rapidly into a narrow ravine
561 in the middle of the runout path (iteration $t=40$ in Figure 9). At the Rocky Mountains site, in addition to standing

562 trees, the forward momentum of the runout may have also restricted lateral spread of the observed runout. Modelled
563 runout is consistently too wide.

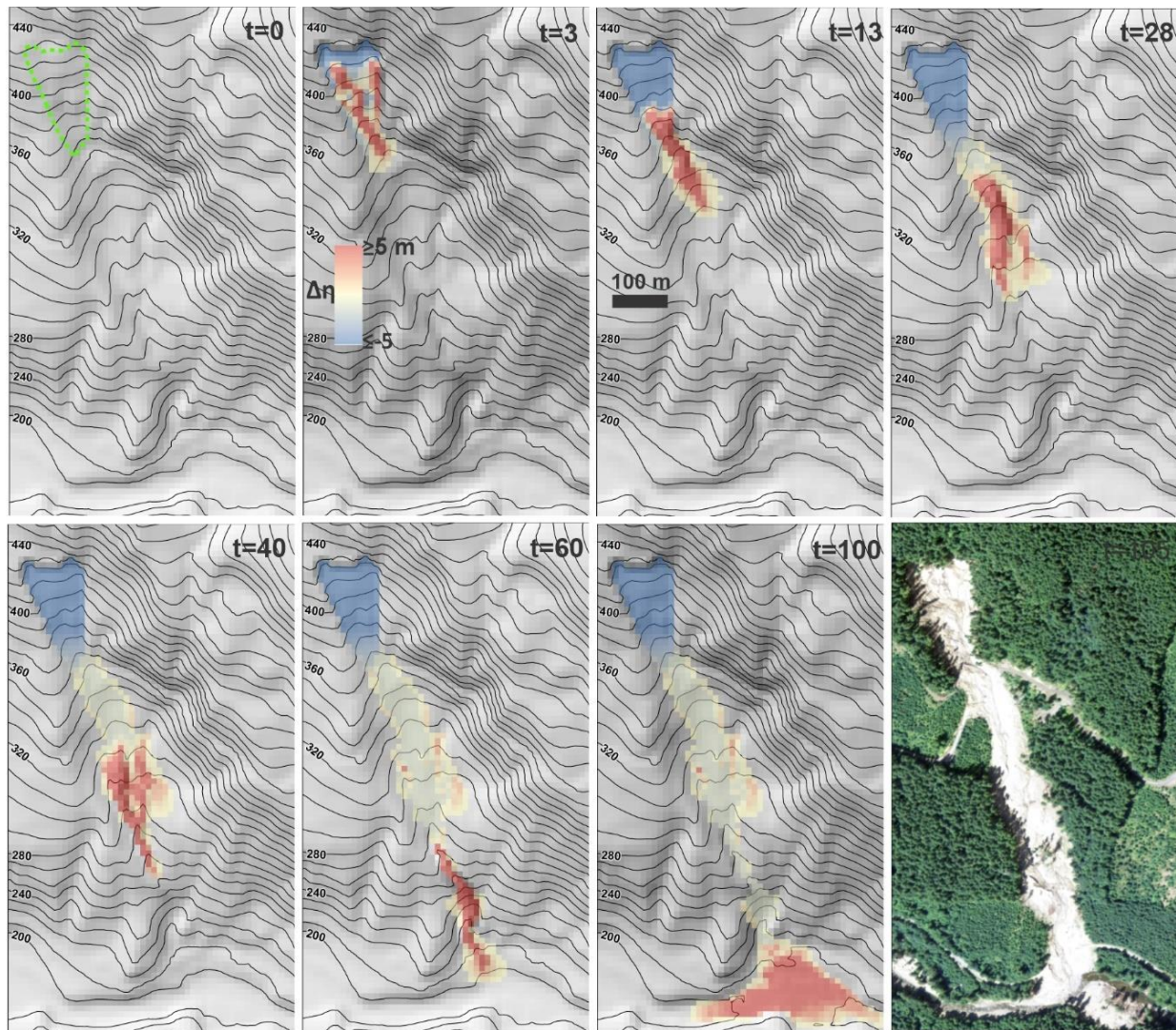
564 Overall, calibration was best at the Cascade Mountain, 2009 landslide (values of Ω_T are highest and values of $\Delta\eta_E$
565 and Q_{sE} are lowest) and poorest at the Rocky Mountain and Olympic Mountain sites (Values of Ω_T are lowest Q_{sE}
566 and $\Delta\eta_E$ are highest). At both the Rocky Mountain and Olympic Mountain sites, because we lacked repeat lidar, we
567 created the DoD from a map of field estimated erosion and deposition depths and estimated the pre-event DEM. The
568 lower calibration scores may indicate that field estimated DoDs were not as accurate as those determined via lidar
569 differencing. Another source of uncertainty that we have not addressed in our study is regolith thickness. Using
570 spatially accurate regolith thickness, rather than a uniform thickness, would likely improve MWR performance too.
571 Nonetheless, although imperfect, at most sites, MWR does not appear to have a strong systematic bias in modeled
572 output, which suggests that MWR may not have any structural weaknesses; however the consistent over-estimated
573 width on planar to divergent topography at the Rocky Mountain site requires further investigation at similar sites to
574 determine if this issue is due to calibration or the model.

575



577
 578
 579
 580
 581
 582

Figure 8. Calibrated model performance as indicated by modeled runout extent, profile plots of Q_s , and reported values of Ω_T , $\Delta\eta_E$ and Q_{sE} . In all maps, up is north except in (e), north is towards the left. (a) Cascade Mountains, 2009; (b) Cascade Mountains, 2022; (c) Black Hills, North; (d) Black Hills, South; (e) Rocky Mountains; (f) Olympic Mountains.

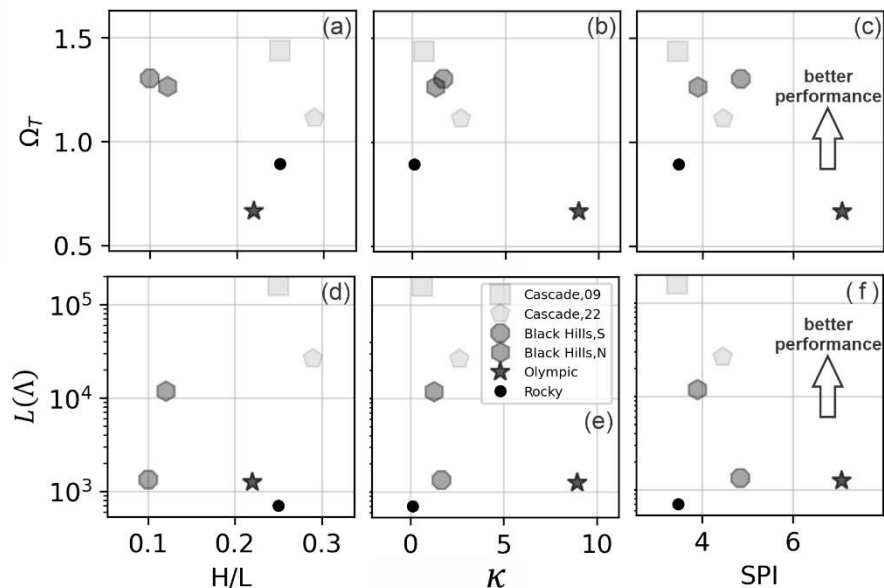


583

584 **Figure 9.** Illustration of modeled runout at the Cascade Mountains, 2009 landslide. At iteration $t = 0$, Algorithm 1
 585 determines the direction and flux of the initial debris over the slip surface of the landslide (all nodes located in
 586 the landslide green-dashed polygon). Note how the landslide slip surface directs the initial flow. In later iterations,
 587 Algorithm 2 routes the debris down slope, updating the debris and the terrain. By the end of the modeled
 588 runout, a colluvial fan forms at the base of the slope. Topography lines reflect the underlying terrain, which is
 589 updated after each iteration. MWR successfully replicates diverging flow at iteration $t = 28$ but misses a region of
 590 the observed runout path at iteration $t = 40$ where momentum likely controlled flow direction (compare to runout
 591 scar in air photo and underestimated region on topographic bench in Figure 8a)

592 To understand whether the ability to calibrate MWR systematically varies with topography of the runout path, we
 593 compared model performance with three topographic indices described by Chen & Yu (2011). The indices are
 594 computed from the terrain in the observed runout extent and include the relief ratio (H/L), mean total curvature (κ)
 595 and the mean specific stream power index (SPI). The index H/L equals the average slope of the runout path (or relative
 596 relief), determined as the total topographic relief of the runout (measured from the center of the landslide to the end
 597 of the runout path) divided by the horizontal length of the runout and indicates the mobility of the runout. Index κ
 598 represents topographic convergence, which is the second derivative of the terrain surface, with increasingly positive

599 values of index κ reflecting growing topographic convergence and concave-up channel profile (e.g., Istanbulluoglu et
600 al., 2008). The index SPI is determined as the natural log of the product of the contributing area and slope. Indices κ
601 and SPI are computed at each node in the runout extent and the mean values are computed from all nodes in the extent.
602 Comparison of model performance with respect to the topographic indices in Figure 10 shows: slightly improved
603 model performance over runout-paths that are less convergent (SPI and κ values of the observed runout path are
604 lower) and on steeper terrain (higher H/L) but neither trend is significant. The latter finding appears to be mostly a
605 result of how well modelled sediment transport and topographic change (Q_{sE} and $\Delta\eta_E$) replicated observed, as there
606 does not appear to be a trend in Ω_T with H/L and the two best performing models (both Cascade Mountain landslides)
607 had the lowest (best) Q_{sE} values and low $\Delta\eta_E$ values. Both findings are likely impacted by the grid size we used to
608 represent terrain. As noted above, at all sites we used a 10-m grid, but at some sites 10-m doesn't quite capture the
609 relief of channelized topography that controlled observed runout, leading to modelled runout that was considerably
610 wider than observed and causing low Ω_T value (this is especially true at the Olympic Mountains site, Figure 10a, b
611 and c).
612 In summary, using the calibration utility, we showed how the MWR can be calibrated to a range of different landslide
613 types and runout terrains. To a certain degree, though calibration, MWR can be parameterized to compensate for
614 deficiencies in the DEM or processes not explicitly represented in the model (momentum, woody debris). We were
615 unable to establish a clear pattern between calibration performance and topographic indices. This finding is likely
616 because numerous factors other than the terrain form, such as the DEM resolution, the quality of the DoD and
617 importance of processes not explicitly included in the model also impact performance.
618



619
620 **Figure 10.** Illustration of model calibration, as reflected by the posterior parameter likelihood $L(\theta)$ and planimetric
621 fit (Ω_T) relative to topographic indices. There is no strong trend between the topographic indices and calibration
622 performance.

623 6. Discussion

624 6.1 Strategic testing of MWR for hazard mapping applications

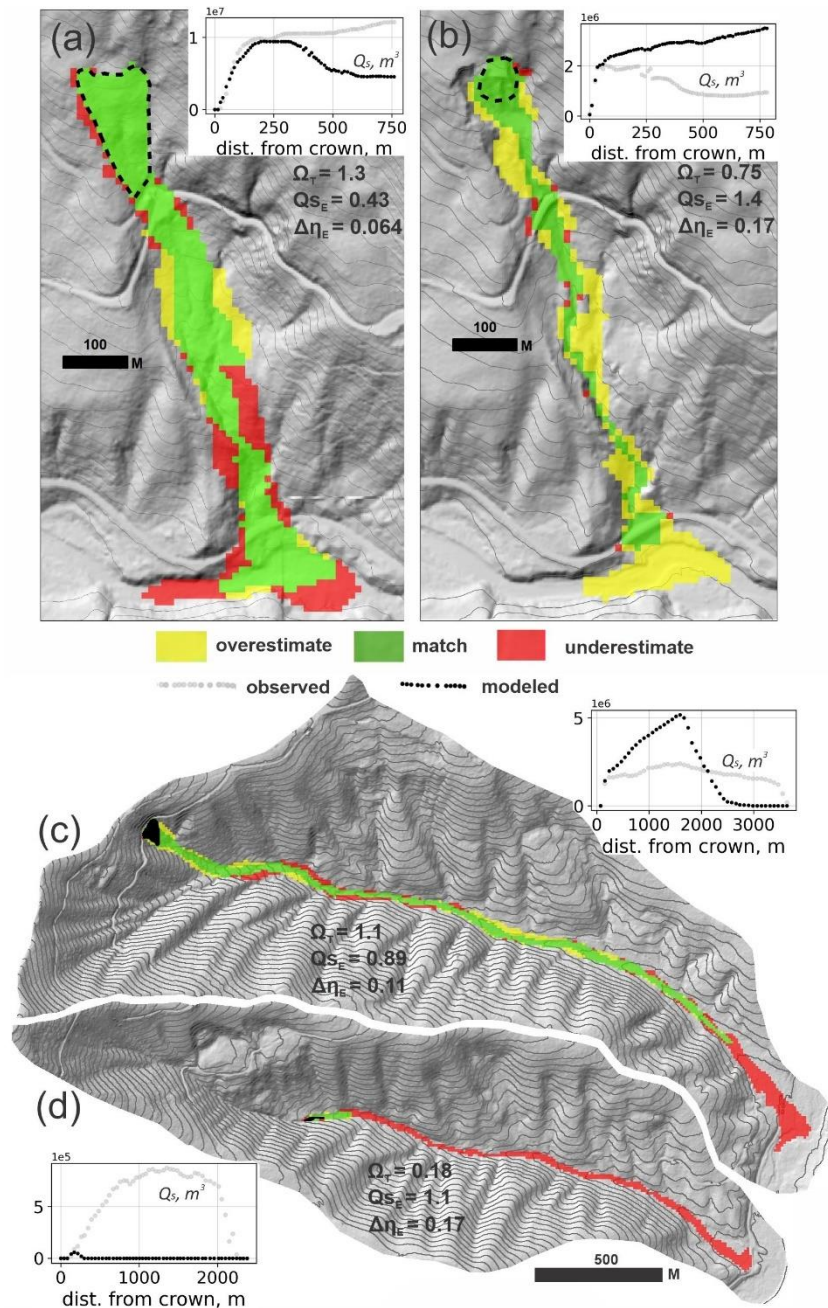
625 Having demonstrated basic model response to topography and that MWR can be calibrated to a variety of landslides
626 and runout terrains, we now strategically test MWR using the Cascade Mountain and Black Hills sites. Since both of
627 these sites include two separate landslides, we can thus test model performance by swapping best-fit model parameters
628 at each site, rerunning the models and comparing results with the original, calibrated results. At the Cascade Mountain
629 site, the 2009 and 2022 landslides originated on the same hillslope (Figure 8a and 8b). At Black Hills site, the two
630 landslides occurred on different hillslopes but in adjacent east-west oriented watersheds (Figure 8c and 8d).

631 As shown in Figure 11, at three of the landslides (both Cascade Mountain landslides and the Black Hills, North
632 landslide), when the best-fit parameters from the other landslide are used to predict runout, the accuracy of modelled
633 runout planimetric extent drops but resultant Ω_T values can still be as high or higher than values reported in other
634 studies (compare to equivalent Ω_T values in Gorr et al., 2022 and Barnhart et al., 2021). In terms of modelled sediment
635 transport and topographic change, swapping best-fit parameters has a more substantial effect. At the Cascade
636 Mountain, 2009 landslide, using the 2022 best-fit parameter values causes about half of the modelled runout material
637 to prematurely deposit on the hillslope, reducing the amount of sediment that reaches the valley floor (Q_{sE} increases
638 by a factor of nine; Figure 11). Using the Cascade Mountain, 2009 parameter values on the Cascade Mountain, 2022
639 landslide (Figure 11b) increases modelled runout extent and results in nearly four times the entrainment and transport
640 of sediment to the valley floor, causing Q_{sE} to increase by a factor of 20 and $\Delta\eta_E$ by 83%. At the Black Hills site,
641 using the South basin best-fit model parameters at the North basin causes Q_{sE} and $\Delta\eta_E$ increase by 83% and 39%
642 respectively (Figure 11c). Unlike the other three landslides, swapping best-fit parameters at the Black Hills, South
643 landslide results in both large sediment transport and runout extent error because the North basin best-fit parameters
644 cause modelled landslide to entrain too little and stop only a few hundred meters from the initial source area (Figure
645 11d).

646 Although the need for calibration of MWR is a limitation for its transferability across sites, this limitation holds true
647 for most physics-based models. Barnhart et al. (2021) compared the ability of three different detailed-mechanistic
648 models to replicate an observed post-wildfire debris-flow runout event in California, USA. All three models used a
649 shallow-water-equation-based approach that conserved both mass and momentum, representing the flow as either a
650 single phase or double phase fluid. All models gave comparable results in simulating the event, suggesting that there
651 may not be a “true” best model. Despite the high level of detail and processes explicitly included in each model, all
652 models were sensitive to and required an estimate of the total mobilized volume, and the ability to replicate observed
653 runout ultimately depended on the selection of the parameters used to characterize debris flow properties.

654

655



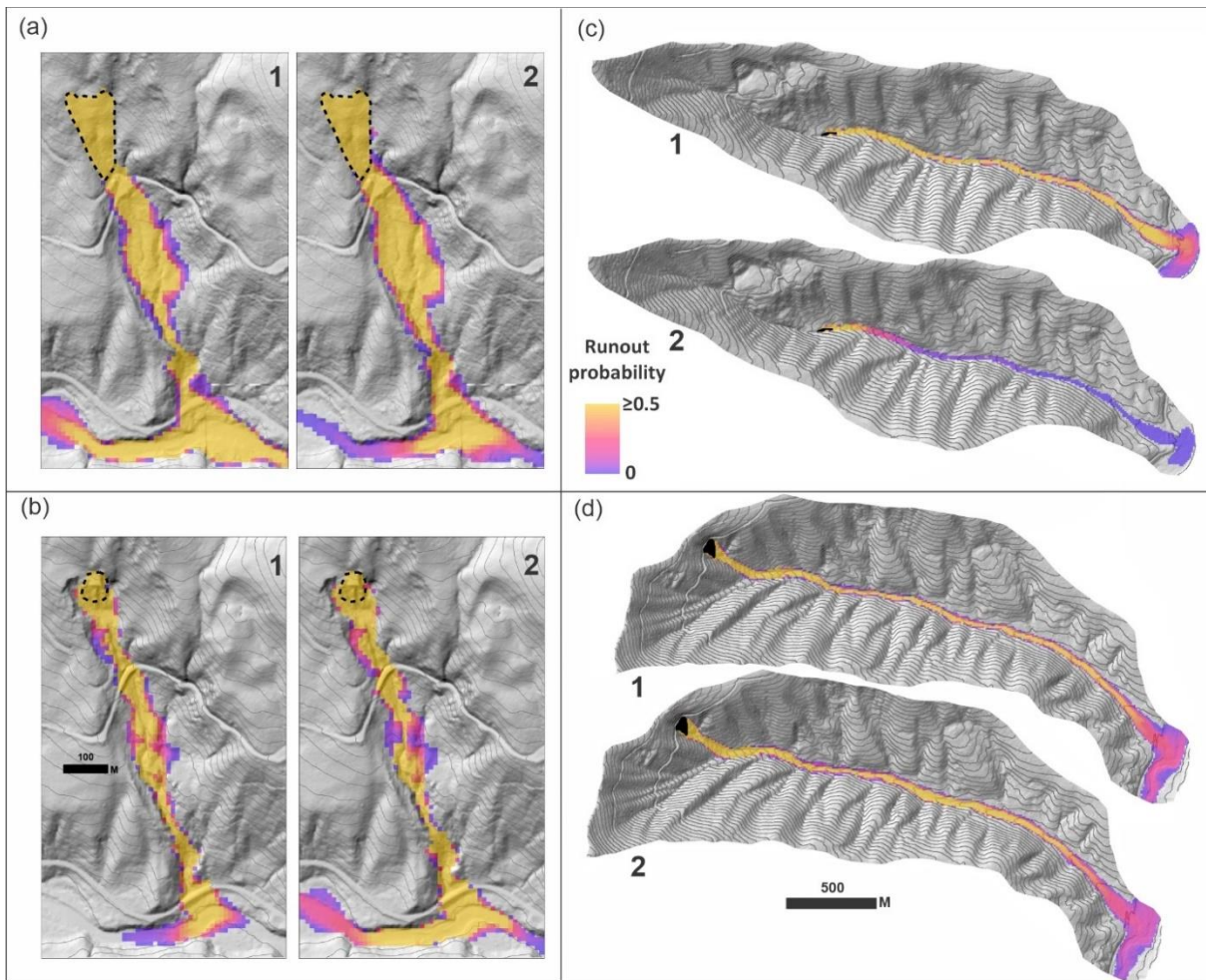
656

657 **Figure 11.** Model performance using the neighboring landslide parameter values, as indicated by modeled runout
 658 extent, profile plots of Q_s , reported values of Ω_T , $\Delta\eta_E$ and Q_{SE} . Compare with Figure 8. (a) Cascade Mountain,
 659 2009; (b) Cascade Mountain, 2022; (c) Black Hills, North; (d) Black Hills, South

660

661 As landslide hazard models often forecast hazard probabilistically, an alternative test to simply swapping the best-fit
 662 parameters is to swap parameter PDFs determined from the calibration utility and compare probability of runout at
 663 each model node (equation 30). As shown in Figure 12, similar to the first test, at three of the landslides, using the
 664 parameter distribution associated with the neighbouring landslide results in relatively minor changes in whether runout

665 is likely to occur versus not occur (probability of runout $\geq 50\%$; Figures 12a, 12b and 12d). At the Black Hills South
666 landslide, swapping parameter PDFs causes a large change in runout probability (Figure 12c).
667



668 **Figure 12.** Model tests by swapping parameter PDFs and comparing runout probability at the (a) Cascade Mountain,
669 2009; (b) Cascade Mountain, 2022; (c) Black Hills, South and; (d) Black Hills, North sites. (1) runout using
670 parameter distributions of the site and (2) runout using parameter distributions of the neighboring site.
671
672

673 The results of these two tests suggest that in most cases, once best-fit parameters or parameter PDFs have been
674 established for a landslide, those parameter/PDF values may be useful for assessing runout extent but not useful for
675 sediment transport and topographic change prediction at nearby sites. However, we suspect that these results are a
676 consequence of comparing very different landslide types and runout processes. In regions where landslide processes
677 are relatively uniform (like the Olympic Mountain site), calibration to one landslide might be sufficient to predict the
678 depositional patterns of another. At sites like the Cascade Mountain and Black Hills sites, which consisted of a diverse
679 range of landslide processes including small, confined debris flows to large, unconfined debris avalanches, MWR may
680 need to be calibrated to each type of landslide and predictive applications might involve applying the appropriate
681 parameter set based on landslide type.

682 **6.2. MassWastingRunout probability applications**

683 In this section we briefly demonstrate how to determine runout probability from a probabilistically determined
684 landslide hazard map or a specific, potentially unstable slope using MWR. The first application may be appropriate
685 for watershed- to regional-scale runout hazard assessments. The second application is an example hazard assessment
686 for a potentially unstable hillslope. Both applications are demonstrated at the Olympic Mountain site where landslide
687 size and type tended to be relatively uniform and parameter PDFs determined through calibration may therefore
688 represent typical runout processes in the basin.

689 **6.2.1. Runout probability from a landslide hazard map**

690 To determine runout probability from a landslide hazard map, we ran MWR Probability using option 3, reading a
691 series of mapped landslide source areas created by an externally run Monte Carlo landslide initiation model. For the
692 landslide initiation model, we used LandslideProbability, an existing component in Landlab that computes landslide
693 probability by iteratively calculating Factor-of-Safety (FS : ratio of the resisting to the driving forces) at each node on
694 the raster model grid Np times from randomly selected soil (regolith) hydrology properties (e.g., soil depth, saturated
695 hydraulic conductivity) soil strength (friction angle, cohesion) and recharge rates (precipitation input rate minus
696 evapotranspiration and soil storage). Landslide probability at a node is defined as the number of times $FS < 1$ divided
697 by Np .

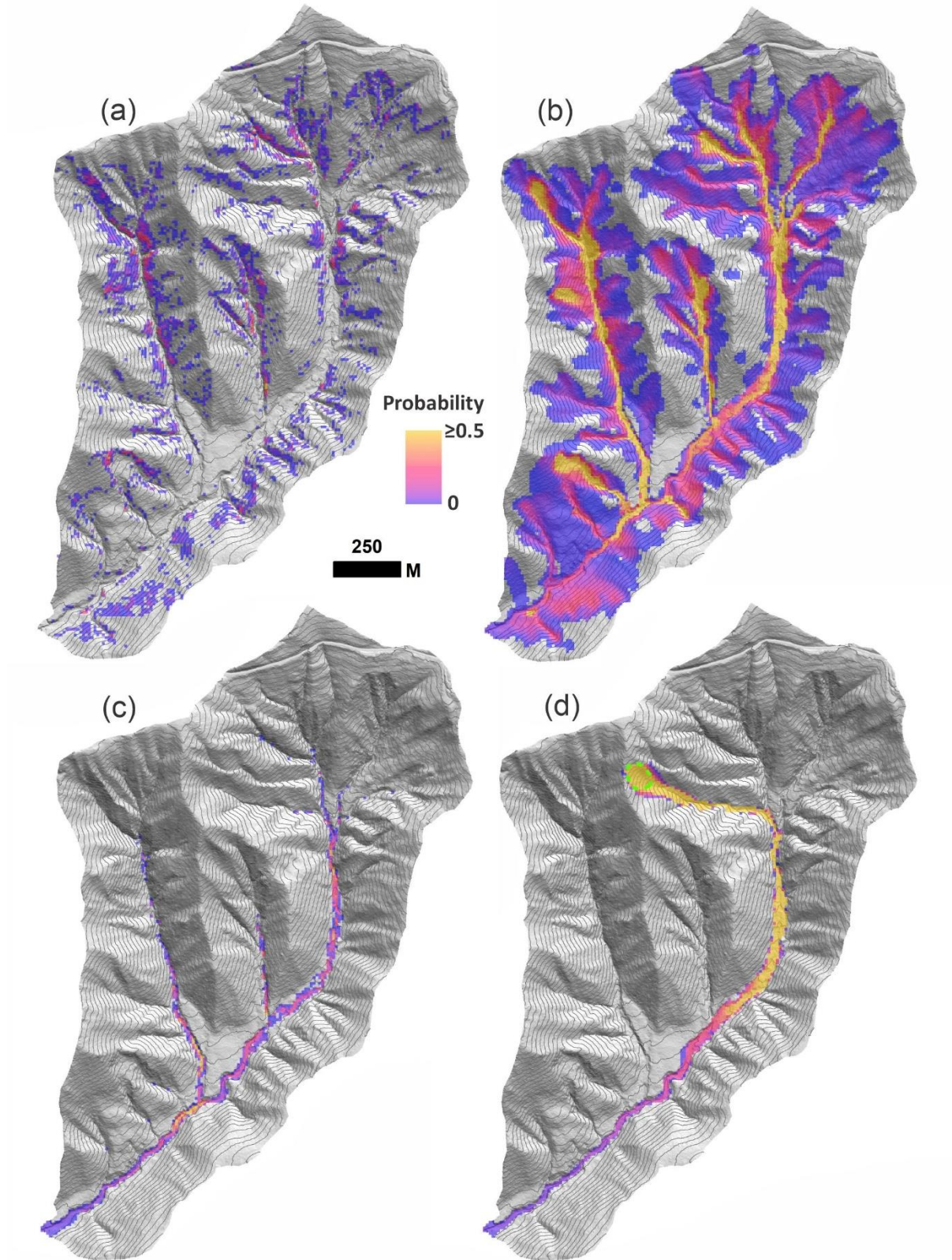
698 We first ran LandslideProbability using a 50-year precipitation event (WRCC, 2017) to determine landslide
699 probability (Figure 13a) over the entire Olympic Mountains model domain and create the series of Np FS maps.
700 Details on the LandslideProbability setup are included in the Supplementary Material. We then read the series of FS
701 maps into MWR Probability, treating all nodes with $FS < 1$ as a landslide source, and ran MWR Np times. Each
702 iteration, MWR read a new FS map and randomly selected a new set of parameter values from S_c - q_c parameter PDFs
703 created by the calibration utility.

704 Runout probability results are illustrated in Figure 13b and show that the probability of runout is high in many of the
705 second order channels but low at the basin outlet. As discussed in Section 3, the probability of aggradation or erosion
706 caused by the runout can also be determined by adjusting the numerator of (30) and the probability of deposition
707 greater than 1 meter is shown in Figure 13c. In this example, in addition to MWR parameter uncertainty, runout
708 probability reflects uncertainty in landslide size and location caused by a 50-year precipitation event.

709 **6.2.2 Runout probability for a specific, potentially unstable slope**

710 When field evidence or other data indicate that a specific hillslope may be potentially unstable, but the exact area of
711 a potential landslide on that slope is unknown, MWR can be used to generate a hazard estimate that takes into account
712 the uncertainty in the landslide area. For this application, MWR Probability is run using option (2), which requires a
713 polygon representing the extent of the potentially unstable slope. For each model repetition, a landslide area can form
714 anywhere within the potentially unstable slope and is at least as large as a user defined minimum size but no larger
715 than the potentially unstable slope.

716 As an example application of using MWR Probability option (2), we designated a 0.6 ha, convergent hillslope in the
717 headwaters of the Olympic Mountains site as a potentially unstable slope and modelled runout probability, again using
718 $Np = 1000$ (Figure 13d). This example shows that, given uncertainty in the landslide size and location, and
719 uncertainty in calibrated parameterization of MWR, if a landslide were to initiate on the potentially unstable slope,
720 the probability of the runout reaching the basin outlet is less than 5%.



721
 722 **Figure 13.** Olympic Mountain site: (a) Landslide probability, $P(FS \leq 1)$. (b) Corresponding runout probability,
 723 $P(\Delta\eta)$. (c) Probability of deposition greater than 1 m and (d) Runout probability for the potentially unstable slope
 724 (green-dashed polygon).

725 **7.0 Concluding remarks**

726 In this study, we described, calibrated and tested MassWastingRunout (MWR), a new cellular-automata landslide
727 runout model that combines the functionality of simple runout algorithms used in landscape evolution and watershed
728 sediment yield models (WSMs) with the predictive detail typical of runout models used for landslide inundation hazard
729 mapping. MWR is implemented in Python as a component for the Landlab earth surface modelling toolkit and is
730 designed for probabilistic landslide hazard assessments, sediment transport and landscape evolution applications.
731 MWR includes a Markov Chain Monte Carlo calibration utility that determines the best-fit parameter values for a site
732 as well as empirical Probability Density Functions (PDF) of the parameter values. MWR also includes a utility called
733 MWR Probability that takes the PDF output from the calibration utility to model runout probability.

734 Results show that despite its simple conceptualization, MWR can replicate observed erosion, deposition and sediment
735 transport patterns. A notable finding of this paper is that MWR modeled runout did not have any strong systematic
736 bias in predictions (toward unrealistically short or wide flows, for example), which suggests that MWR may not have
737 any structural weaknesses. When compared to other models capable of replicating inundation patterns of observed
738 runout events, the strength of MWR lies in its potential computation efficiency, use of field-inferable parameters,
739 limited reliance on calibration parameters (only two, critical slope, S_c , and a threshold flux for deposition, q_c) and its
740 ability to internally estimate the total mobilized volume. MWR needs only the location and geometry of an initial
741 source area to model the entire runout process.

742 MWR shows a rich set of intuitive responses to topographic curvature and slope and model performance over a range
743 of landslide and landscape conditions across the four sites we used for this study was sufficiently controlled with the
744 two calibration parameters. When calibrated to each individual site, the volumetric error of MWR, $\Delta\eta_E$, ranged
745 between 6% and 15% (median 9.1%) of the observed total mobilized volume. Except for the Rocky Mountains site
746 where MWR consistently modelled wider-than-observed flow, the cumulative flow error along the runout profile
747 (Q_{sE}) were limited to 5%-19% of the mean cumulative flow determined from the observed DoD. These are considered
748 acceptable levels of performance given that the total mobilized volume of many debris flow models assume an order
749 of magnitude range of confidence.

750 Once MWR is calibrated to runout observations, it can be linked to other landslide hazard models and may be useful
751 as a regional runout hazard mapping tool in areas with relatively uniform landslide processes. In this study we showed
752 how to use MWR to map debris flow hazard for an expert-defined potentially unstable slope and for a landslide hazard
753 map produced from an externally run Monte Carlo landslide initiation model (Figure 13).

754 As a component of the Landlab earth surface modelling toolkit, MWR is designed to be compatible with other models.
755 MWR can be readily coupled with a landslide initiation model (e.g., LandslideProbability) and geomorphic transport
756 laws for hillslope diffusion and fluvial incision to investigate the role of landslides and their runout on long-term
757 landscape evolution. We did not explore the use of MWR in landscape evolution or sediment yield models in this
758 study, however its ability to replicate observed topographic change and sediment transport at multiple sites shows
759 promise for this application. The use of a calibrated runout model in WSMs might allow for region-specific and more
760 insightful predictions of landslide impact on landscape morphology and watershed-scale sediment dynamics.

761

762 **8.0 Notation**

763	q_{R_i}	[m]	debris flux from a node to each of the node i -th receiver nodes
764	q_O	[m]	the total out-going debris flux
765	Nr		the number of receiving nodes of node n
766	S_i		the underlying topographic slope ($\tan \theta$) to each of the node i -th receiver nodes
767	a		exponent in (1) that controls how flow is distributed to downslope nodes
768	q_I	[m]	The total incoming flux
769	Nd		number of donors nodes to a node
770	q_{D_j}	[m]	the flux from node D_j (the j -th donor node)
771	h	[m]	flow depth at node, adjusted to be no more than h_{max}
772	h_{max}	[m]	the maximum observed flow depth
773	A	[m]	aggradation depth
774	S_c		critical slope
775	S		steepest slope to the node's eight neighbouring nodes
776	Δx	[m]	cell length
777	$A_{p N_a}$	[m]	potential aggradation depth that forms a deposit that spreads over N_a consecutive nodes
778	$A_{p,i}$	[m]	i -th deposition amount in the deposit illustrated in Figure 4
779	N_a		number of nodes q_s^I is assumed to spreads over
780	E	[m]	erosion depth
781	h_r	[m]	regolith depth
782	h_e	[m]	potential erosion depth
783	θ	[°]	topographic slope used to determine shear stress, equal to $\tan^{-1}(S)$
784	τ	[Pa]	basal shear stress
785	τ_c	[Pa]	critical shear stress of the regolith
786	k		erodibility parameter in (11)
787	f		exponent, controls the non-linearity of h_e in (11)
788	ρ	[kg/m ³]	density of runout material
789	σ	[Pa]	normal stress at basal surface
790	φ		tangent of collision angle between grains, measured from the vertical axis
791	v_s		volumetric solids concentration
792	ρ_s	[kg/m ³]	density of solids
793	D_s	[m]	characteristic particle diameter
794	u	[m/s]	depth average flow velocity
795	z	[m]	depth below the flow surface
796	u^*		shear velocity
797	g	[m/s]	acceleration due to gravity
798	$\Delta\eta$	[m]	change in elevation at node
799	ξ_D		attribute value delivered to the node
800	ξ_R		attribute value sent to receiver nodes
801	ξ		attribute value at node
802	Λ		parameter set
803	$L(\Lambda)$		likelihood of parameter set
804	$p(\Lambda)$		prior probability of parameter set
805	Ω_T		omega metric, nondimensional
806	α	[m ²]	modelled area of matching extent (compared to observed runout extent)
807	β	[m ²]	modelled area of overestimated extent
808	γ	[m ²]	modelled area of underestimated extent
809	$\Delta\eta_E$		volumetric error of the modelled topographic change relative to the observed total
810			mobilized volume, fraction.
811	V	[m ³]	observed total mobilized volume
812	p		the number of nodes in the modelled runout extent
813	$\Delta\eta_{Mi}$	[m]	the modelled topographic change [m] at the i -th node within the runout extent
814	$\Delta\eta_{Oi}$	[m]	the observed topographic change [m] at the i -th node within the runout extent

815		
816	Q_{sE}	mean-modelled-cumulative flow error along the runout path relative to the observed
817		mean cumulative flow, fraction.
818	Q_{sj}	[m ³] the cumulative debris flow volume (Q_s) at each node, j ,
819	$\Delta\eta_{ij}$	[m] the topographic change [m] at the i -th node located upstream of node j
820	u_j	the total number of all nodes located upstream of j
821	$\overline{Q_{so}}$	[m ³] the observed mean cumulative flow
822	$P(\Delta\eta)$	probability of runout at a model node
823	Np	number Monte Carlo iterations used to determine probability

824 9.0 Acknowledgements

825 This research was partially supported by the following programs: National Science Foundation (NSF)
826 PREEVENTS program, ICER-1663859; NSF OAC-2103632; and NASA Grant number 22-RRNES22-
827 0010 and benefited from critical referee reviews. Stephen Slaughter field reviewed the Cascade
828 Mountains, 2009 and Black Hills landslides the year they occurred and provided photos and field
829 observations that aided interpretation. John Jenkins helped with the 2022 field reconnaissance the
830 Cascade Mountains landslide. Eli Schwat helped with field reconnaissance at the Olympic Mountains site.
831 This work also benefitted from Landlab support and coding guidance from Eric Hutton and helpful
832 feedback from many others.

833 10.0 Competing interests

834 The contact author has declared that none of the authors has any competing interests.

835

836 11.0 References

- 837 Bagnold, R. A.: Experiments on a gravity-free dispersion of large solid spheres in a Newtonian fluid under shear.
838 Proceedings of the Royal Society of London, 225(1160), 49–63. <https://doi.org/10.1098/rspa.1954.0186>, 1954.
- 839 Barca, D., Crisci, G., Di Gregorio, S., and Nicoletta, F.: Cellular automata method for modelling lava flows:
840 Simulation of the 1986–1987 eruption, Mount Etna, Sicily, in Kilburn, C., and Luongo, G., eds., Active lavas:
841 Monitoring and modeling: London, University College of London Press, p. 291–309, 1993.
- 842 Barnhart, K. R., Hutton, E. W. H., Tucker, G. E., Gasparini, N. M., Istanbuluoglu, E., Hopley, D. E. J., Lyons, N. J.,
843 Mouchene, M., Nudurupati, S. S., Adams, J. M., & Bandaragoda, C.: Short communication: Landlab v2.0: a software
844 package for Earth surface dynamics. *Earth Surface Dynamics*, 8(2), 379–397. [https://doi.org/10.5194/esurf-8-379-](https://doi.org/10.5194/esurf-8-379-2020)
845 [2020](https://doi.org/10.5194/esurf-8-379-2020), 2020.
- 846 Barnhart, K. R., Jones, R., George, D. J., McArdell, B. W., Rengers, F. K., Staley, D. M., & Kean, J. W.: Multi-Model
847 Comparison of Computed Debris Flow Runout for the 9 January 2018 Montecito, California Post-Wildfire Event.
848 *Journal of Geophysical Research: Earth Surface*, 126(12). <https://doi.org/10.1029/2021jf006245>, 2021.

849 Benda, L., & Dunne, T.: Stochastic forcing of sediment supply to channel networks from landsliding and debris flow.
850 *Water Resources Research*, 33(12), 2849–2863. <https://doi.org/10.1029/97wr02388>, 1997.

851 Benda, L., Veldhuisen, C. P., & Black, J.: Debris flows as agents of morphological heterogeneity at low-order
852 confluences, Olympic Mountains, Washington. *Geological Society of America Bulletin*, 115(9), 1110.
853 <https://doi.org/10.1130/b25265.1>, 2003.

854 Beven, K.: A manifesto for the equifinality thesis. *Journal of Hydrology*, 320(1–2), 18–36.
855 <https://doi.org/10.1016/j.jhydrol.2005.07.007>, 2006.

856 Burton, A., & Bathurst, J. C.: Physically based modelling of shallow landslide sediment yield at a catchment scale.
857 *Environmental Geology*, 35(2–3), 89–99. <https://doi.org/10.1007/s002540050296>, 1998.

858 Bigelow, P., Benda, L., Miller, D., & Burnett, K. M.: On Debris Flows, River Networks, and the Spatial Structure of
859 Channel Morphology. *Forest Science*, 53(2), 220–238. <https://doi.org/10.1093/forestscience/53.2.220>, 2007

860 Campforts, B., Shobe, C. M., Overeem, I., & Tucker, G. E.: The Art of Landslides: How Stochastic Mass Wasting
861 Shapes Topography and Influences Landscape Dynamics. *Journal of Geophysical Research: Earth Surface*, 127(8).
862 <https://doi.org/10.1029/2022jf006745>, 2022

863 Campforts, B., Shobe, C. M., Steer, P., Vanmaercke, M., Lague, D., & Braun, J.: HyLands 1.0: a hybrid landscape
864 evolution model to simulate the impact of landslides and landslide-derived sediment on landscape evolution.
865 *Geoscientific Model Development*, 13(9), 3863–3886. <https://doi.org/10.5194/gmd-13-3863-2020>, 2020.

866 Capart, H., & Fraccarollo, L.: Transport layer structure in intense bed-load. *Geophysical Research Letters*, 38(20),
867 n/a. <https://doi.org/10.1029/2011gl049408>, 2011.

868 Capart, H., Hung, C., & Stark, C. R.: Depth-integrated equations for entraining granular flows in narrow channels.
869 *Journal of Fluid Mechanics*, 765. <https://doi.org/10.1017/jfm.2014.713>, 2015.

870 Carretier, S., Martinod, P., Reich, M., & Godd eris, Y.: Modelling sediment clasts transport during landscape evolution.
871 *Earth Surface Dynamics*, 4(1), 237–251. <https://doi.org/10.5194/esurf-4-237-2016>, 2016.

872 Chase, C. G.: Fluvial landsculpting and the fractal dimension of topography. *Geomorphology*, 5(1–2), 39–57.
873 [https://doi.org/10.1016/0169-555x\(92\)90057-u](https://doi.org/10.1016/0169-555x(92)90057-u), 1992.

874 Chen, C., & Yu, F.: Morphometric analysis of debris flows and their source areas using GIS. *Geomorphology*, 129(3–
875 4), 387–397. <https://doi.org/10.1016/j.geomorph.2011.03.002>, 2011.

876 Chen, H., & Zhang, L.: EDDA 1.0: integrated simulation of debris flow erosion, deposition and property changes.
877 *Geoscientific Model Development*, 8(3), 829–844. <https://doi.org/10.5194/gmd-8-829-2015>, 2015.

878 Chen, T.-Y. K., Wu, Y.-C., Hung, C.-Y., Capart, H., and Voller, V. R.: A control volume finite-element model for
879 predicting the morphology of cohesive-frictional debris flow deposits, *Earth Surface Dynamics*, 11, 325–342,
880 <https://doi.org/10.5194/esurf-11-325-2023>, 2023.

881 Clerici, A., & Perego, S.: Simulation of the Parma River blockage by the Corniglio landslide (Northern Italy).
882 *Geomorphology*, 33(1–2), 1–23. [https://doi.org/10.1016/s0169-555x\(99\)00095-1](https://doi.org/10.1016/s0169-555x(99)00095-1), 2000.

883 Codd, E. F.: *Cellular Automata* (1st ed.). New York, Academic Press, 1968.

884 Coz, J. L., Renard, B., Bonnifait, L., Branger, F., & Boursicaud, R. L.: Combining hydraulic knowledge and uncertain
885 gaugings in the estimation of hydrometric rating curves: A Bayesian approach. *Journal of Hydrology*, 509, 573–587.
886 <https://doi.org/10.1016/j.jhydrol.2013.11.016>, 2014.

887 Crave, A., & Davy, P.: A stochastic “precipiton” model for simulating erosion/sedimentation dynamics. *Computers
888 & Geosciences*, 27(7), 815–827. [https://doi.org/10.1016/s0098-3004\(00\)00167-9](https://doi.org/10.1016/s0098-3004(00)00167-9), 2001.

889 D’Ambrosio, D., Di Gregorio, S., Iovine, G., Lupiano, V., Rongo, R., & Spataro, W.: First simulations of the Sarno
890 debris flows through Cellular Automata modelling. *Geomorphology*, 54(1–2), 91–117. [https://doi.org/10.1016/s0169-555x\(03\)00058-8](https://doi.org/10.1016/s0169-555x(03)00058-8), 2003.

892 Egashira, S., Honda, N., & Itoh, T.: Experimental study on the entrainment of bed material into debris flow. *Physics
893 and Chemistry of the Earth, Parts a/B/C*, 26(9), 645–650. [https://doi.org/10.1016/s1464-1917\(01\)00062-9](https://doi.org/10.1016/s1464-1917(01)00062-9), 2001.

894 Foglia, L., Hill, M. C., Mehl, S. W., and Burlando, P. (2009), Sensitivity analysis, calibration, and testing of a
895 distributed hydrological model using error-based weighting and one objective function, *Water Resources
896 Research*, 45, W06427, doi:10.1029/2008WR007255.

897 Fannin, R. J., & Wise, M. P.: An empirical-statistical model for debris flow travel distance. *Canadian Geotechnical
898 Journal*, 38(5), 982–994. <https://doi.org/10.1139/t01-030>, 2001.

899 Frank, F., McArdell, B. W., Huggel, C., & Vieli, A.: The importance of entrainment and bulking on debris flow runoff
900 modeling: examples from the Swiss Alps. *Natural Hazards and Earth System Sciences*, 15(11), 2569–2583.
901 <https://doi.org/10.5194/nhess-15-2569-2015>, 2015.

902 Freeman, T. G.: Calculating catchment area with divergent flow based on a regular grid. *Computers &
903 Geosciences*, 17(3), 413–422. [https://doi.org/10.1016/0098-3004\(91\)90048-i](https://doi.org/10.1016/0098-3004(91)90048-i), 1991.

904 Gartner, J. E., Cannon, S. H., & Santi, P. M.: Empirical models for predicting volumes of sediment deposited by debris
905 flows and sediment-laden floods in the transverse ranges of southern California. *Engineering Geology*, 176, 45–56.
906 <https://doi.org/10.1016/j.enggeo.2014.04.008>, 2014.

907 Gelman, A., Carlin, J. B., Stern, H. S., Dunson, D. B., Vehtari, A., & Rubin, D. B.: *Bayesian Data Analysis* (3rd ed.).
908 Electronic Edition, 2021.

909 Goode, J. R., Luce, C. H., & Buffington, J. M.: Enhanced sediment delivery in a changing climate in semi-arid
910 mountain basins: Implications for water resource management and aquatic habitat in the northern Rocky Mountains.
911 *Geomorphology*, 139–140, 1–15. <https://doi.org/10.1016/j.geomorph.2011.06.021>, 2012.

912 Gorr, A., McGuire, L. A., Youberg, A., & Rengers, F. K.: A progressive flow-routing model for rapid assessment of
913 debris-flow inundation. *Landslides*, 19(9), 2055–2073. <https://doi.org/10.1007/s10346-022-01890-y>, 2022

914 Guthrie, R., Hockin, A., Colquhoun, L., Nagy, T., Evans, S. G., & Ayles, C. P.: An examination of controls on debris
915 flow mobility: Evidence from coastal British Columbia. *Geomorphology*, 114(4), 601–613.
916 <https://doi.org/10.1016/j.geomorph.2009.09.021>, 2010.

917 Guthrie, R. H., & Befus, A. D.: DebrisFlow Predictor: an agent-based runout program for shallow landslides. *Natural*
918 *Hazards and Earth System Sciences*, 21(3), 1029–1049. <https://doi.org/10.5194/nhess-21-1029-2021>, 2021.

919 Hammond C.J., Prellwitz R.W., Miller S.M.: Landslides hazard assessment using Monte Carlo simulation. In: Bell
920 DH (ed) *Proceedings of 6th international symposium on landslides*, Christchurch, New Zealand, Balkema, vol 2. pp
921 251–294, 1992.

922 Han, Z., Chen, G., Li, Y., Tang, C., Xu, L., He, Y., Huang, X., & Wang, W.: Numerical simulation of debris-flow
923 behavior incorporating a dynamic method for estimating the entrainment. *Engineering Geology*, 190, 52–64.
924 <https://doi.org/10.1016/j.enggeo.2015.02.009>, 2015.

925 Han, Z., Li, Y., Huang, J., Chen, G., Xu, L., Tang, C. Y., Zhang, H., & Shang, Y.: Numerical simulation for run-out
926 extent of debris flows using an improved cellular automaton model. *Bulletin of Engineering Geology and the*
927 *Environment*, 76(3), 961–974. <https://doi.org/10.1007/s10064-016-0902-6>, 2017.

928 Han, Z., Ma, Y., Li, Y., Zhang, H., Chen, N., Hu, G., & Chen, G.: Hydrodynamic and topography based cellular
929 automaton model for simulating debris flow run-out extent and entrainment behavior. *Water Research*, 193, 116872.
930 <https://doi.org/10.1016/j.watres.2021.116872>, 2021.

931 Heiser, M., Scheidl, C., & Kaitna, R.: Evaluation concepts to compare observed and simulated deposition areas of
932 mass movements. *Computational Geosciences*, 21(3), 335–343. <https://doi.org/10.1007/s10596-016-9609-9>, 2017.

933 Hobley, D. E. J., Adams, J. M., Nudurupati, S. S., Hutton, E. W. H., Gasparini, N. M., Istanbuluoglu, E., & Tucker,
934 G. E.: Creative computing with Landlab: an open-source toolkit for building, coupling, and exploring two-dimensional
935 numerical models of Earth-surface dynamics. *Earth Surface Dynamics*, 5(1), 21–46. [https://doi.org/10.5194/esurf-5-](https://doi.org/10.5194/esurf-5-21-2017)
936 [21-2017](https://doi.org/10.5194/esurf-5-21-2017), 2017.

937 Horton, P., Jaboyedoff, M., Rudaz, B., & Zimmermann, M. N.: Flow-R, a model for susceptibility mapping of debris
938 flows and other gravitational hazards at a regional scale. *Natural Hazards and Earth System Sciences*, 13(4), 869–885.
939 <https://doi.org/10.5194/nhess-13-869-2013>, 2013.

940 Hungr, O., Morgan, G. J., & Kellerhals, R.: Quantitative analysis of debris torrent hazards for design of remedial
941 measures. *Canadian Geotechnical Journal*, 21(4), 663–677. <https://doi.org/10.1139/t84-073>, 1984.

942 Hungr, O., & Evans, S. G.: Entrainment of debris in rock avalanches: An analysis of a long run-out mechanism.
943 *Geological Society of America Bulletin*, 116(9), 1240. <https://doi.org/10.1130/b25362.1>, 2004.

944 Hutter, K., Svendsen, B., & Rickenmann, D.: Debris flow modeling: A review. *Continuum Mechanics and*
945 *Thermodynamics*, 8(1), 1–35. <https://doi.org/10.1007/bf01175749>, 1996.

946 Iovine, G., D'Ambrosio, D., & Di Gregorio, S.: Applying genetic algorithms for calibrating a hexagonal cellular
947 automata model for the simulation of debris flows characterised by strong inertial effects. *Geomorphology*, 66(1–4),
948 287–303. <https://doi.org/10.1016/j.geomorph.2004.09.017>, 2005.

949 Istanbuluoglu, E. Bras R. L.: Vegetation-modulated landscape evolution: Effects of vegetation on landscape
950 processes, drainage density, and topography. *Journal of Geophysical Research*, 110(F2).
951 <https://doi.org/10.1029/2004jf000249>, 2005.

952 Istanbuluoglu, E., Bras R. L., Flores-Cervantes, H., and Tucker, G. E.: Implications of bank failures and fluvial
953 erosion for gully development: Field observations and modeling, *J. Geophysical Research*, 110, F01014,
954 doi:10.1029/2004JF000145, 2005.

955 Istanbuluoglu, E., O. Yetemen, E. R. Vivoni, H. A. Gutierrez-Jurado, and R. L. Bras, Eco-geomorphic implications
956 of hillslope aspect: Inferences from analysis of landscape morphology in central New Mexico, *Geophysical. Research*
957 *Letters*, 35, L14403, 10.1029/ 2008GL034477, 2008.

958 Iverson, R. M.: The physics of debris flows. *Reviews of Geophysics*, 35(3), 245–296.
959 <https://doi.org/10.1029/97rg00426>, 1997.

960 Iverson, R. M., & Denlinger, R. P.: Flow of variably fluidized granular masses across three-dimensional terrain: 1.
961 Coulomb mixture theory. *Journal of Geophysical Research*, 106(B1), 537–552.
962 <https://doi.org/10.1029/2000jb900329>, 2001.

963 Iverson, R.M., How should mathematical models of geomorphic processes be judged?. In Wilcock, P., & Iverson, R.
964 (Eds.), *Prediction in Geomorphology*. American Geophysical Union, 2003.

965 Julien, P. Y., & Paris, A.: Mean Velocity of Mudflows and Debris Flows. *Journal of Hydraulic Engineering*, 136(9),
966 676–679. [https://doi.org/10.1061/\(asce\)hy.1943-7900.0000224](https://doi.org/10.1061/(asce)hy.1943-7900.0000224), 2010.

967 Kean, J. W., Staley, D. M., Lancaster, J., Rengers, F., Swanson, B., Coe, J., et al.: Inundation, flow dynamics, and
968 damage in the 9 January 2018 Montecito debris-flow event, California, USA: Opportunities and challenges for post-
969 wildfire risk assessment. *Geosphere*, 15(4), 1140–1163. <https://doi.org/10.1130/GES02048.1>, 2019

970 Korup, O.: Effects of large deep-seated landslides on hillslope morphology, western Southern Alps, New Zealand.
971 *Journal of Geophysical Research*, 111(F1). <https://doi.org/10.1029/2004jf000242>, 2006

972 Lancaster, S. T., Hayes, S. K., & Grant, G. E.: Effects of wood on debris flow runout in small mountain watersheds.
973 *Water Resources Research*, 39(6). <https://doi.org/10.1029/2001wr001227>, 2003.

974 Larsen, I. J., & Montgomery, D. R.: Landslide erosion coupled to tectonics and river incision. *Nature Geoscience*,
975 5(7), 468–473. <https://doi.org/10.1038/ngeo1479>, 2012.

976 Liu, J., Wu, Y., Gao, X., & Zhang, X.: A Simple Method of Mapping Landslides Runout Zones Considering Kinematic
977 Uncertainties. *Remote Sensing*, 14(3), 668. <https://doi.org/10.3390/rs14030668>, 2022.

978 Major, J. J.: Depositional Processes in Large-Scale Debris-Flow Experiments. *The Journal of Geology*, 105(3), 345–
979 366. <https://doi.org/10.1086/515930>, 1997.

980 Major, J. J., & Iverson, R. M.: Debris-flow deposition: Effects of pore-fluid pressure and friction concentrated at flow
981 margins. *Geological Society of America Bulletin*, 111(10), 1424–1434. [https://doi.org/10.1130/0016-7606\(1999\)111](https://doi.org/10.1130/0016-7606(1999)111),
982 1999.

983 McCoy, S. W., Kean, J. W., Coe, J. A., Tucker, G. S., Staley, D. M., & Wasklewicz, T. A.: Sediment entrainment by
984 debris flows: In situ measurements from the headwaters of a steep catchment. *Journal of Geophysical Research*,
985 117(F3), n/a. <https://doi.org/10.1029/2011jf002278>, 2012.

986 McDougall, S., & Hungr, O.: A model for the analysis of rapid landslide motion across three-dimensional terrain.
987 *Canadian Geotechnical Journal*, 41(6), 1084–1097. <https://doi.org/10.1139/t04-052>, 2004.

988 Medina, V., Hürlimann, M., & Bateman, A.: Application of FLATModel, a 2D finite volume code, to debris flows in
989 the northeastern part of the Iberian Peninsula. *Landslides*, 5(1), 127–142. [https://doi.org/10.1007/s10346-007-0102-](https://doi.org/10.1007/s10346-007-0102-3)
990 [3](https://doi.org/10.1007/s10346-007-0102-3), 2008.

991 Montgomery, D. R., & Dietrich, W. E.: Where do channels begin? *Nature*, 336(6196), 232–234.
992 <https://doi.org/10.1038/336232a0>, 1988.

993 Murray, B.A., & Paola, C.: A cellular model of braided rivers. *Nature*, 371(6492), 54–57.
994 <https://doi.org/10.1038/371054a0>, 1994.

995 Murray, A. B., & Paola, C.: Properties of a cellular braided-stream model. *Earth Surface Processes and Landforms*,
996 22(11), 1001–1025. [https://doi.org/10.1002/\(sici\)1096-9837\(199711\)22:11](https://doi.org/10.1002/(sici)1096-9837(199711)22:11), 1997.

997

998 Murray A.B.: Which Models Are Good (Enough), and When?. In: John F. Shroder (ed.) *Treatise on Geomorphology*,
999 Volume 2, pp. 50-58. San Diego: Academic Press, 2013.

1000 Natural Resources Conservation Service | Snow and Water Interactive Map (n.d.). Natural Resources Conservation
1001 Service. <https://www.nrcs.usda.gov/resources/data-and-reports/snow-and-water-interactive-map>, Accessed April,
1002 2022

1003 Nudurupati, S. S., Istanbuloglu, E., Tucker, G. E., Gasparini, N. M., Hobley, D. E. J., Hutton, E. W. H., Barnhart,
1004 K. R., & Adams, J. M.: On transient semi-arid ecosystem dynamics using Landlab: vegetation shifts, topographic
1005 refugia, and response to climate. *Water Resources Research*, 59(4). <https://doi.org/10.1029/2021wr031179>, 2023.

1006 Perron, J. T.: Climate and the Pace of Erosional Landscape Evolution. *Annual Review of Earth and Planetary Sciences*,
1007 45(1), 561–591. <https://doi.org/10.1146/annurev-earth-060614-105405>, 2017.

1008 Reid, M. J., Coe, J. A., & Brien, D. L.: Forecasting inundation from debris flows that grow volumetrically during
1009 travel, with application to the Oregon Coast Range, USA. *Geomorphology*, 273, 396–411.
1010 <https://doi.org/10.1016/j.geomorph.2016.07.039>, 2016.

1011 Renard, B., Garreta, V., & Lang, M. J.: An application of Bayesian analysis and Markov chain Monte Carlo methods
1012 to the estimation of a regional trend in annual maxima. *Water Resources Research*, 42(12).
1013 <https://doi.org/10.1029/2005wr004591>, 2006.

1014 Rengers, F. K., McGuire, L. A., Kean, J. W., Staley, D. M., and Hobbey, D. E. J.: Model simulations of flood and
1015 debris flow timing in steep catchments after wildfire, *Water Resources Research*, 52, 6041–6061,
1016 doi:10.1002/2015WR018176, 2016.

1017 Roda-Boluda, D. C., D'Arcy, M., McDonald, J., & Whittaker, A. C.: Lithological controls on hillslope sediment
1018 supply: insights from landslide activity and grain size distributions. *Earth Surface Processes and Landforms*, 5), 956–
1019 977. <https://doi.org/10.1002/esp.4281>, 2018.

1020 Shaller, P. J., Doroudian, M., & Hart, M. W.: The Eureka Valley Landslide: Evidence of a dual failure mechanism for
1021 a Long-Runout Landslide. *Lithosphere*, 2020(1). <https://doi.org/10.2113/2020/8860819>, 2020.

1022 Schürch, P., Densmore, A. L., Rosser, N., & McArdeell, B. W.: Dynamic controls on erosion and deposition on debris-
1023 flow fans. *Geology*, 39(9), 827–830. <https://doi.org/10.1130/g32103.1>, 2011.

1024 Shen, P., Zhang, L. M., Wong, H., Peng, D., Zhou, S., Zhang, S., & Chen, C.: Debris flow enlargement from
1025 entrainment: A case study for comparison of three entrainment models. *Engineering Geology*, 270, 105581.
1026 <https://doi.org/10.1016/j.enggeo.2020.105581>, 2020.

1027 Stock, J. P. J., & Dietrich, W. E.: Erosion of steepland valleys by debris flows. *Geological Society of America Bulletin*,
1028 118(9–10), 1125–1148. <https://doi.org/10.1130/b25902.1>, 2006.

1029 Strauch, R. L., Istanbuluoglu, E., Nudurupati, S. S., Bandaragoda, C., Gasparini, N. M., & Tucker, G. E.: A
1030 hydroclimatological approach to predicting regional landslide probability using Landlab. *Earth Surface Dynamics*,
1031 6(1), 49–75. <https://doi.org/10.5194/esurf-6-49-2018>, 2018.

1032 Takahashi, T.: *Debris Flow* (2nd ed.). CRC Press, Taylor & Francis Group, 2014.

1033 Tucker, G. E., & Bras, R. L.: Hillslope processes, drainage density, and landscape morphology. *Water Resources*
1034 *Research*, 34(10), 2751–2764. <https://doi.org/10.1029/98wr01474>, 1998.

1035 Tucker, G. E., Hancock, G. J.: Modelling landscape evolution. *Earth Surface Processes and Landforms*, 35(1), 28–50.
1036 <https://doi.org/10.1002/esp.1952>, 2010.

1037 Tucker, G. E., McCoy, S., & Hobbey, D. E. J.: A lattice grain model of hillslope evolution. *Earth Surface Dynamics*,
1038 6(3), 563–582. <https://doi.org/10.5194/esurf-6-563-2018>, 2018.

1039 Western Regional Climate Center. (n.d.), from <https://wrcc.dri.edu/>, accessed 2017 and 2022

1040 Whipple, K. X., & Dunne, T.: The influence of debris-flow rheology on fan morphology, Owens Valley, California.
1041 *Geological Society of America Bulletin*, 104(7), 887–900. [https://doi.org/10.1130/0016-7606\(1992\)104](https://doi.org/10.1130/0016-7606(1992)104), 1992.

1042 Zhou, G. G. D., Li, S., Song, D., Choi, C. E., & Chen, X.: Depositional mechanisms and morphology of debris flow:
1043 physical modelling. *Landslides*, 16(2), 315–332. <https://doi.org/10.1007/s10346-018-1095-9>, 2019.

1044

1045